Paleoproterozoic manganese oxide precipitation in oxic seawater surface and reductive enrichment in anoxic seafloor

Felipe Holanda dos Santos[a,b]; Wagner da Silva Amaral[b]; Ernest Chi Fru[c]; Ana Clara Braga de Souza[d], Alice Bosco-Santos[b]

[a] Institute of Geosciences and Engineering, Federal University of Western Pará (UFOPA), Santarém, Pará, Brazil
[b] Institute of Geosciences, University of Campinas (UNICAMP), Campinas, São Paulo, Brazil
[c] Centre for Geobiology and Geochemistry, School of Earth and Environmental Sciences, Cardiff University, United Kingdom
[d] Geology Graduate Program (PPGG), Federal University of Ceará (UFC), Fortaleza, Ceará, Brazil

Abstract

Accelerated precipitation of Mn-rich rocks in the early Paleoproterozoic ocean is considered to reflect the irreversible rise of oxygen in the atmosphere during the Great Oxidation Event (GOE), 2.501-2.220 billion years ago. But the precipitation conditions, pathways, mechanisms, and linkages to ocean redox, broadly remain unresolved. The Lagoa do Riacho Mn deposit in Borborema Province, northeastern Brazil, Ceará state, consists mainly of manganese-rich and manganese-poor silicates deposited during the GOE epoch. Negative Ce anomalies in the manganese-poor silicates point to the scavenging of Ce^{3+} onto Mn-oxyhydroxide reactive surfaces in the oxygenated surface waters. In contrast, samples with positive Ce anomalies, predominantly associated with the manganese-rich silicates, indicate a reductive dissolution of Mn-oxyhydroxides across a redoxcline, enriching the anoxic bottom water with Ce and Mn^{2+}. A paleoredox reconstruction based on couple Mn, Mo, and U systematics supports the existence of the proposed Mn-oxide redox shuttle that enriched the anoxic sediment pile with Mn precipitated from the oxygenated shallow surface waters. This study uncovers a unique pathway in Paleoproterozoic Mn mineralization involving the transfer of Mn oxides from an oxygenated upper ocean reservoir to a predominantly deep anoxic silicate reservoir that was subsequently metamorphosed. The proposed Mn oxide sink switch mechanism is different from the commonly reported reductive transfer of Mn to a diagenetic carbonate sink during the Paleoproterozoic.

Keywords: Manganese-rich rocks; Paleoproterozoic; Great Oxidation Event; Borborema Province; Redoxcline

1. Introduction

The Paleoproterozoic, spanning 2.5-1.6 billion years ago (Ga) was a time of environmental, biogeochemical and tectonic upheavals (Kirschvink et al., 2000; Bekker et al., 2004, 2006; Bakker and Holland 2012; Lyons et al., 2014; Chi Fru et al., 2015, 2016, 2019; Gumsley et al., 2017; Javaux and Lepot, 2018). Expansion of oxygenic photosynthesis is believed to have driven the Great Oxidation Event (GOE between 2.501-2.220 Ga, Canfield et al., 2013; Bekker, 2014; Lyons et al., 2014), leading oxygen to concentrated permanently in the atmosphere to exceed 10^{-5} present day atmospheric levels (PAL) compared to the preceding Archean interval (Karhu and Holland, 1996; Holland, 2006; Lyons et al., 2014; Warke et al., 2020; Poulton et al., 2021). Geochemical evidence for the unprecedented atmospheric oxygen accumulation is the disappearance of mass-independent fractionation of sulfur isotopes (MIF-S) in sedimentary pyrite, the lack of detrital pyrite and uraninite in fluvial and deltaic sediments and the increasing enrichment of Fe in paleosols, after 2.501 Ga (Farquhar et al., 2000; Lyons et al., 2014; Warke et al., 2020). The accumulation of redox-sensitive metals (e.g., Mo and U enrichments) and metalloids in marine sediments, including global-scale precipitation of manganese and iron oxides, are also evidence for a major ocean redox change (e.g., Roy, 2006; Scott et al., 2008; Maynard, 2010; Partin et al., 2013a, 2013b; Lyons et al., 2014; Chi Fru et al., 2016, 2019; Robbins et al., 2016; Konhauser et al., 2017). At this time, novel oxidative biogeochemical pathways probably emerged due to increased electron acceptor availability as nitrate, sulfate concentration and arsenate concentration (e.g., Kah et al., 2004; Zerkle et al., 2017; Chen et al., 2020; Chi Fru et al., 2019).

Although more than 60% of the global manganese deposition through time occurred during the GOE timespan (Roy, 2006; Maynard, 2010; Johnson et al., 2016), suggesting a correlation with the biological turnover, the specific mechanisms that led to intense manganese oxidation and precipitation are not yet fully understood. Possibilities include (i) the oxidation of Mn^{2+} by molecular O_2 or its derivatives, such as superoxides (Calvert and Pedersen, 1996; Post, 1999; Tebo et al., 2005; Johnson, 2015); (ii) biological mediated reactions by anoxygenic phototrophs where Mn^{2+} acts as an electron donor (Johnson et al., 2013; Daye et al., 2019); and (iii) UV-catalyzed photochemical oxidation by ultraviolet (UV) radiation without contributions from life or O_2 (Anbar and Holland, 1992, Liu et al., 2020). Further transformation of the primary Mn oxides to carbonate minerals by early diagenetic processes in some sedimentary settings, like the Franceville Basin in Gabon (Leclerc and Weber, 1980; Gauthier-Lafaye and Weber, 2003; Beukes et al., 2016), has been interpreted to reflect a redoxcline (Okita et al., 1988; Maynard et al., 2010; Beukes et al., 2016; Ossa Ossa et al., 2018; Mayika et al., 2020).

Therefore, the designated mechanisms, anoxic or oxic, for the deposition of Mn deposits in marine sediments, is an important proxy for dimension and reconstructing Earth's surface oxygenation during the Paleoproterozoic, a matter of intense debate (Lyons et al., 2014, 2020; Hodgskiss and Sperling, 2021; Poulton et al., 2021).

The hypothesis of a global oxygen catastrophe across the GOE that resulted in a radical transition from globally anoxic to globally oxic habitats was unlikely given the geological evidence for the pace of oxygenation, which better supports the "Canfield Ocean" model of a protracted period of an intermediate ocean oxidation state (Canfield 1998; Canfield et al., 2000). Oxygen accumulation probably began in localized and isolated shallow-waters before gradually expanding (on the timescale of millions of years) into the global marine photic zone and into relatively deeper waters (Canfield et al., 2008). Here, on a detailed geochemical examination of manganese-bearing rocks from the Borborema Province, northeastern Brazil, we provide novel insights on Paleoproterozoic redox ocean reconstruction. Our results support ocean redox shifts that are temporally related to the Lomagundi-Jatuli Event, in the GOE aftermath, among the most important records for enhanced primary productivity in the Paleoproterozoic (*c.f.* Bekker et al., 2006; Melezhik et al., 2007; Kump et al., 2011; Bekker and Holland, 2012; Bekker, 2014).

2. Geological setting

2.1. Borborema Province

The Borborema Province of the Northeast Brazil region lay adjacent to the West African Congo and São Francisco cratons before the opening of the Atlantic Ocean, following the breakup of West Gondwana during Phanerozoic times (Caby, 1989; Castaing et al., 1994; Brito Neves et al., 2000; Neves, 2003; De Wit et al., 2008; Fig. 1A-B). In this context, the Borborema Province represents Gondwana's westernmost segment (Torsvik and Cocks, 2013).

The significantly voluminous Palaeoproterozoic rocks in the Borborema Province overlying the Archean tonalite-trondhjemite-granodiorite (TTG) basement (Fetter 1999; Dantas et al. 2013; Ganade et al., 2017), consist predominantly of orthogneisses, migmatites and diverse metasedimentary rocks (Fetter et al., 2000; Hollanda et al., 2011; Souza et al., 2016; Costa et al., 2018). A series of Meso- to Neoproterozoic granitic bodies, supracrustal rocks and shear zones (e.g., Patos, Pernambuco, and Transbrasiliano) developed towards the end of the Neoproterozoic Era, are common in this locality (Vauchez et al. 1995; Neves and Mariano 1999; Viegas et al. 2014; Fig. 1B).

A proposal has been made to divide the Borborema Province into three major structural

domains, namely (1) the Northern Borborema Province, including the Médio Coreaú, Ceará Central, and the Rio Grande do Norte domains; (2) the Central Domain; and (3) the Southern Domain (Brito Neves et al., 2000). The Northern Borborema Province, which is the focus of this study, comprises an expressive Rhyacian granitic and gneissic belt, as well as related metavolcanic–sedimentary sequences of the same proposed age hosting the manganese-rich rocks studied here (Fetter et al., 2000; Hollanda et al., 2011; Garcia et al., 2014; Costa et al., 2015; Souza et al., 2016; Calado et al., 2019).

2.2. Manganese mineralization from Northern Borborema Province

Several manganese-rich sequences occur for at least 70 km along a N-NE trending linear belt within the Paleoproterozoic units of the Northern Borborema Province (Souza and Ribeira Filho, 1983; Gomes, 2013; Costa and Palheta, 2017). These manganese-rich rocks, in many cases containing up to 40 wt% MnO_2, are interbedded with amphibolite facies metamorphic rocks, including graphitic pelites, garnet-bearing quartzites, meta-wackes, meta-conglomerates and calc-silicate rocks (Souza and Ribeira Filho, 1983; Gomes, 2013). Manganese-bearing minerals consist predominantly of rhodochrosite ($Mn^{2+}CO_3$), spessartine ($Mn_2^{3+}Al_2[SiO_4]_3$), rhodonite-pyroxmangite (Mn^{2+}, Fe^{2+}, Mg, Ca, SiO_4), and tephroite ($Mn^{2+}{}_2SiO_4$), along with non-manganese minerals such as graphite (C), pyrite ($Fe^{2+}S_2$) and pyrrhotite ($[Fe^{2+}]_{1-x}S$). Massive ores record localized supergene enrichment to manganese ores with pyrolusite, manganite ($Mn^{3+}O[OH]$), cryptomelane, and todorokite ($[Na,Ca,K,Ba,Sr]_{1-x}[(Mn,Mg,Al]_6O_{12}\cdot nH_2O$ (Souza and Ribeira Filho, 1983; Gomes, 2013).

For this study, we use the Lagoa do Riacho manganese deposit within the manganese mineralization trend (Fig. 1C). The Lagoa do Riacho is the largest Mn deposit from the Northern Borborema Province where Mn ore is extracted from three open-pit mines. Furthermore, the most occurrence of manganese-rich rocks from the Borborema Province comes from out-crop samples, which are weathered and with some degree of supergene alteration. Thus, the Lagoa do Riacho manganese deposit was studied as a representative site for drill-core sampling and analysis. At this deposit, post-metamorphic changes related to the supergene enrichment of silicate manganese minerals are recorded mainly at the top of the drill cores and evidenced by the presence of late oxides and hydroxides (e.g., pyrolusite and cryptomelane) (Santos et al., 2021). The manganese mineralization in the Lagoa do Riacho manganese deposit is hosted within the Canindé do Ceará Complex, which is subdivided into (1) paragneisses and schist layers, interbedded with marbles, quartzites, calc-silicate rocks, amphibolites, and manganese- and iron formations; and (2) orthogneisses of granitic to tonalitic

composition and subordinate amphibolites (Fetter et al., 2000; Castro, 2004; Torres et al., 2007; Costa and Palheta, 2017) (Fig. 2B).

The U-Pb detrital zircon ages obtained for the high-grade metasedimentary rocks of the Canindé do Ceará Complex mostly fall between 2.2 and 1.9 Ga (Kalsbeek et al., 2013; Costa and Palheta, 2017), which are very similar to the 2.2-1.9 Ga U-Pb zircon ages of the associated orthogneisses (Fetter et al., 1999; Castro, 2004; Garcia et al., 2014; Costa and Palheta, 2017). Close to the Canindé do Ceará Complex, a 2.1 arc-related mafic outcrop and intermediate volcanic-plutonic rocks, are hosts to Mn-rich silicate rocks (Fetter, 1999; Martins et al., 2009; Costa et al., 2015; Sousa et al., 2019). To the east of the Canindé do Ceará Complex, in the neighboring Jaguaretama Complex, a migmatite paragneiss hosting Mn-rich rocks, and petrographically similar to sample #10029 of the present study, yielded a U-Pb zircon age of 2046 Ma, is interpreted to coincide with the timing of high-grade metamorphic transformation of the sedimentary protolith (Calado et al., 2019). In addition, further south to the study area and in the same Mn mineralization trend of the Northern Borborema Province, migmatized orthogneisses hosting manganese silicate rocks have yielded a U-Pb isochron at ca. 2046 Ma (Gomes, 2013). All these constrains support a Paleoproterozoic age for manganese mineralization in this region, consistent with the age of the vast Lagoa do Riacho Mn deposit dated in the present study.

3. Material and methods

3.1 Sampling

A total of twenty manganese-bearing rocks from drill cores Ocr-1, 4 and 8 were selected for whole-rock geochemical analyses (Appendix Table 1). These rocks were categorized into manganese-rich (silicate manganese rock-SMR) and manganese-poor (manganese-quartzite and garnetite) lithotypes. Fresh rocks, free of alteration, with no evidence of supergene enrichment and without any late hydrothermal feature (e.g., veinlets), were prioritized during sampling.

3.2 Petrography

Petrographic features of representative manganese-bearing drill core samples (Ocr-1, 4 and 8) were investigated on polished thin sections at the Microscopy Laboratory of the Institute of Geosciences, University of Campinas, and in the SEMlab of the Federal University of Ceará, using polarized light on Leica microscope model DM 50P. Common and secondary phases, including pre-, sin- and post-metamorphic minerals and their respective textures, were imaged

at the Federal University of Ouro Preto using a JEOL JXA-8230 super probe operated with an acceleration voltage of 15 kV and a 20 nA beam current.

3.3. Geochemistry

For geochemical analyses performed at ALS Global Laboratories Ltd. (subsidiaries in Minas Gerais, Brazil and Lima, Peru), approximately 400 g of fresh lithotypes were crushed and ground to <200 mesh size with a jaw crusher and agate mill. Rock samples were analyzed for determination of trace (As, Co, Cu, Mo, Ni, Pb, Sc, La, Ce, Pr, Nd, Sm, Gd, Eu, Tb, Dy, Ho, Er, Yb, Lu, Y, Cr, Hf, Nb, Rb, Sr, Ta, Th, Y, V, Zr) and major (Si, Al, Fe, Ca, Mg, Na, K, Cr, Ti, Mn, P, Sr) elements. Concentrations were measured by inductively coupled plasma-atomic emission spectrometry (ICP-AES) or inductively coupled plasma-mass spectrometry (ICP-MS) after chemical treatment (Appendix Table 2). In summary, powdered sample-portions (0.2 g) were digested with multiple acids ($HF + HClO_4 + HCl + HNO_3$), fused with lithium borate, or fused with lithium metaborate/tertraborate, followed by melt dissolution with HNO_3 (5%). Detailed geochemistry methods are available online (www.alsglobal.com).

For chemical and instrumental quality control, certified reference materials of different rock matrices (*GBM908-10* Low Cu Oxide; *GRE-3* Carbonatite; *SY-4* Diorite gneiss; *OREAS-45c* Soil developed over a Ni-Cu-PGE mineralised contact; *OREAS 146* Mineralised REE + Y hornblende-biotite schist; *OREAS 602* Au-Ag-Cu bearing ore blended with argillic rhyodacite; *NCSDC71301* Rock) were analyzed. Reference materials were reported within their recommended ranges (median ± STD), with analytical recoveries from the average value varying between 90 and 109%. Duplicates of selected samples (253A and 247) were analyzed and produced values with deviations under 5% RSD, except for Na_2O that reached 9.8%.

3.3.1 Data management

Due to its low geochemical mobility Al normalizations (key major, minor and trace elements) were used to avoid interpretations on detrital fractions of chemostratigraphy (e.g., Calvert and Pedersen, 1993; Morford and Emerson 1999; Smith et al., 2013). This approach evaluates secular changes on authigenic mineral precipitation and basin-scale redox changes because oxidative weathering promotes the enrichment of highly mobile redox sensitive elements in sediments over poorly mobile ones, like Al, while the supply of detritus by physical weathering does not result in significant fractionation. Normalizations (element/Al) were carried out using the content on the Post-Archean Australian Shale (PAAS) (Taylor and McLennan 1985; McLennan et al., 2001; McLennan, 2001). Furthermore enrichment factors

208 (EF), were calculated according to the equation EF = (element/Al) $_{sample}$/(element/Al) $_{PAAS.}$

209 Enrichments were considered when EF exceeded >2.0 and depletion when values were
210 below <1. Moderate to strong authigenic enrichment is represented by an EF >10 and a
211 moderate to strong authigenic depletion is represented by EF <0.1 (Tribovillard et al. 2006;
212 Algeo and Tribovillard 2009). Appendix Table 3 shows the EFs of the elements of interest
213 considered in this study.
214
215 **3.4. Geochronology**
216 To constrain the depositional age of the sedimentary protolith of the manganese-bearing
217 rocks, one representative sample (#10029) was collected from the base of the drill core Ocr-1
218 and dated by zircon U-Pb geochronology using LA-SF-ICP-MS (Navarro et al., 2017). The
219 medium- to coarse-grained metasedimentary rock is a well-foliated pelite composed of
220 muscovite, feldspar, cordierite, quartz, graphite, garnet, biotite, and sillimanite. It is a graphite-
221 bearing pelitic gneiss hosting manganese.
222 Zircon grains were separated by conventional magnetic and dense liquid techniques.
223 After handpicking, the zircon grains were mounted in epoxy resin and polished. Laser zircon
224 internal structures dating spots were selected after cathodoluminescence (CL) using a SEM
225 operated at 15 kV and a beam current of 6-10 nA at the Laboratory of Isotopic Geology,
226 University of Campinas.
227 A Photon Machines Excite.193 ionization laser system equipped with two HelEx cells
228 was used in combination with a ThermoScientific Element XR ICP-MS, and helium was used
229 as a transporting gas to increase the transport efficiency of the ionized material. The laser spot
230 diameter was 25 μm. Isotopic data processing was performed with the software Iolite (Paton
231 et al., 2010, 2011) and the Visual Age data reduction scheme geochronology (Petrus and
232 Kamber, 2012). All measurements were normalized relative to the international standard zircon
233 reference 91500 of 1065 Ma (Wiedenbeck et al., 1995). An internal standard, the Peixe zircon,
234 which has an LA-ICP-MS U-Pb age of 571 ± 10 Ma (Navarro et al., 2017), was used to track
235 the data reduction routine's quality. Analyses of the 91500-zircon standard resulted in a
236 concordia age of 1063 ± 2 Ma, while Peixe zircon provided a concordia age of 573 ± 3 Ma.
237 The weighted average U-Pb plot, kernel density estimation (KDE) and cumulative
238 probability diagrams were made using the IsoplotR off-line toolbox (Vermeesch, 2018) on
239 RStudio. Initially, only the analyses with concordance higher than 90% were considered in the
240 calculations, following recommendations made by Spencer et al. (2016). Age data and
241 concordia plots were reported at 2σ error. The analyzed dataset of zircon U–Pb analyses are

presented in Appendix Table 4.

4. Results

4.1. Petrography

The manganese-rich lithotype consists of a silicate manganese rock (SMR), whereas the manganese-poor lithologies are grouped into a finely banded garnet-rich rock (garnetite) with minor silicate manganese minerals and a manganese quartzite. The SMR contains tephroite, spessartine-garnet, manganese-pyroxene, and rhodochrosite. At >70%, manganese-pyroxene is the most common silicate in this lithological group (Figure 2A). They appear as up to 6 mm coarser-grained crystals that are sometimes replaced by manganese-amphibole (Figure 2B). Spessartine garnet, the second most abundant mineral, occurs in contact with manganese-pyroxene (Figure 2B and C). Tephroite and carbonate minerals appear in minor volumes (<5%). Other minerals of interest include several sulfides related to chalcopyrite, cobaltite and pyrite (Figure 2D), pyrophanite, graphite, and manganese oxides such as pyrolusite. The sulfide minerals, pyrophanite, and graphite occur in the rock matrix, through foliation planes, in straight contact with the silicate minerals and do not have any relationship with secondary texture fillings and veins (Figure 2C).

The Mn-quartzite rocks are composed primarily of plagioclase, quartz, mica, graphite, and garnet. This group of minerals appears as fine-grained crystals defining a continuous foliation (Figure 2E). In the Mn-quartzite, sulfide also occurs as minor minerals (Figure 2F and G). Abundant and well-developed graphite flakes aligned to the banding, are sometimes in contact with pyrite, covellite and chalcopyrite (Figure 2G). These sulfide minerals have anhedral to subhedral shapes and commonly are medium to fine-grained crystals.

The garnetite occurs as a thinly banded, mm-sized rock showing alternations of garnet and quartz-rich layers. In this lithological group, mica occurs in interstitial areas close to garnet (Figures 2H and I). Another distinguishing feature in this rock, also common in the Mn-quartzite, is the commonly observed alignment of fine millimetric flakes of graphite with the rock matrix, representing primary sedimentary bedding ($S_0//S_1$). Also, similarly to the SMR, carbonate and sulfide minerals appear as minor phases.

4.2. Geochemistry

4.2.1. Major element concentrations

The major element content and enrichment factors for the manganese-rich and manganese-poor silicates are available in Appendix Table 1. The manganese-rich silicates

276 presented MnO concentrations from 22-38 wt%, with Mn_{EF} ranging from 349 to 1101 (Figures
277 3 and 4). SiO_2 and Al_2O_3 concentrations (33-53 wt% and 13-5 wt%, respectively) are minor,
278 compared to concentrations of the manganese-poor silicates. Various other major oxides occur
279 in minor concentrations in the manganese-rich silicates, including Fe_2O_3 (3.5-7.2 wt%), CaO
280 (1.5-5.0 wt%), MgO (0.8-2.9 wt%), TiO_2 (0.1-0.8 wt%) and K_2O, Na_2O and P_2O_5 (generally <
281 0.1 wt%).
282 In the manganese-poor silicates, MnO concentrations and Mn_{EF} range from 0.2-5 wt%
283 and 2.2-82.3, respectively (Figures 3 and 4). SiO_2, Al_2O_3, Fe_2O_3 and Na_2O contents have minor
284 variations of 55.8-61.6 wt%, 14.0-18.6 wt%, 2.6-7.0 wt% and 0.60-4.6 wt%, respectively
285 (Appendix Table 1 and Figure 4). Compared to the manganese-rich silicates, mean negligible
286 CaO concentrations of 0.58 wt% are recorded, while TiO_2 is uniformly low at <0.7 wt%.
287 Often, for the manganese-rich silicates, MnO displays a good negative correlation with
288 SiO_2 (R = - 0.66), a moderate negative correlation with Al_2O_3 (R = -0.46) and a weak negative
289 or absent linear regression with TiO_2 (R= -0.034) and CaO (R= -0.058) (Figure 4). Conversely,
290 in the manganese-poor silicates, MnO shows a strong positive covariance with TiO_2 (R^2 = -
291 0.87) and a moderate positive covariance with CaO (R = 0.5) (Figure 4). For more detail, see
292 correlation matrix plots in figure 4.
293
294 **4.2.2. Redox-sensitive trace element concentrations**
295 Figure 6 displays the relationship between the redox-sensitive trace metal(loids)s Mo,
296 U, V, Co, As, Cr, Cu, and Ni versus MnO, with their corresponding EFs in Figure 3 and
297 Appendix Table 3. The concentration of redox-sensitive trace metals in the manganese-bearing
298 samples shows a broad range.
299 The high enrichment factors of Mo (28-360), Co (18-113), As (4-1542) and Ni (6-58)
300 in the manganese-rich silicates indicate a strong enrichment. Conversely, U_{EF} and Cr_{EF} values
301 of 0.61-2.82 and 0.43-5.23, respectively, are only slightly above PAAS (Figures 3 and 5).
302 Variations in V and Cu are spread with V_{EF} from 2.4-9.3, and Cu_{EF} from 0.4-19.
303 The manganese-poor silicates are also enriched in Mo (1-92) and As (3-84), although
304 to a lesser magnitude relative to the manganese-rich silicates (Figure 5; Appendix Table 3).
305 Average EFs of 3.74 and 3.23 for Co and Ni are similar to each other, while Cr_{EF} of 0.3-2.6, is
306 also slightly minor than for the manganese-rich silicates. Manganese-poor silicates presented
307 an Cu_{EF} of 10-53, U_{EF} of 0.3-1.5 and V_{EF} of 0.9-2.
308
309

310 **4.2.3. Rare-earth element**

311 The Ce, Pr, Eu and La anomalies (*) were calculated following shale-normalization
312 with PAAS (SN) according to previously described linear methods (Bau and Dulski, 1996;
313 Bolhar et al., 2004; Bau and Alexander 2006), using the equations: $(Ce/Ce^*)_{SN}$ = Ce/(2Pr -
314 1Nd); $(Pr/Pr^*)_{SN}$ = Pr/(0.5Ce + 0.5Nd); $(Eu/Eu^*)_{SN}$ = Eu/(0.67Sm + 0.33Tb); and $(La/La^*)_{SN}$
315 = La/(3Pr – 2Nd), respectively.

316 Manganese-bearing rocks REE+Y patterns PAAS normalized are presented in figure 6.
317 The sum of REE+Y (ΣREE+Y) contents for the manganese-rich silicates ranges from 86-357
318 ppm, typically far away from the crustal values of 129 ppm. Sm/Yb_{SN} ratios vary from 0.66 to
319 2.0, reflecting a medium REE (MREE) enrichment, consistent with Sm/Ho ratios and depletion
320 in light REE (LREE), supported by La/Nd ratios compared to the Er/Lu ratios for heavy REEs
321 (HREE) (Figure 6 and Appendix Table 1). There is a range of Eu anomalies, from strongly
322 negative to slightly positive (Eu/Eu_{SN}^* = 0.38-1.27). La_{SN} anomalies are predominantly
323 positive, from 0.84 to 1.36 and Y/Ho_{SN} ratios vary from 0.96 to 1.18. The REE+Y patterns
324 either display a positive Ce anomaly or a lack of positive and negative Ce anomaly (0.88-1.24)
325 (Figures 6 and 7 and Appendix Table 1). $(Pr/Pr^*)_{SN}$ range from 0.90 and 1.05 and.

326 ΣREE+Y content of the manganese-poor silicates is, on average, more abundant than
327 in the manganese-rich silicates, falling within a narrower range from 179.42 to 280.91 ppm.
328 REE patterns are flat or present a slight LREE enrichment (Figure 6). Accordingly, Sm/Yb_{SN}
329 ratios range from 0.61-3.33, averaging 1.26. Eu_{SN} anomaly display variable values, from 0.56-
330 1.50 and all samples presented positive La_{SN} anomaly (0.99 to 1.42), and Y/Ho_{SN} ratios varied
331 from 0.93 to 1.08. The manganese-poor silicates Ce anomalies that span from 0.88-1.11 (Figure
332 7), trend from positive towards negative anomalies, while their associated $(Pr/Pr^*)_{SN}$ anomalies
333 show limited variations from 0.95-1.12.

334

335 **4.3 Geochronology**

336 Representative cathodoluminescence (CL) images of the zircon crystals from the
337 graphite-bearing pelitic gneiss (#10029) investigated in this work are shown in Figure 8,
338 together with the $^{207}Pb/^{206}Pb$ ages and Th/U ratios. Zircon U-Pb analyses are presented in
339 concordia diagrams, probability density plots, histograms and weighted average diagram
340 (Figure 8). For more detail on U–Pb analytical data, see Appendix Table 4.

341 Zircon crystals from the graphite-bearing pelitic gneiss sample (#10029) are colorless,
342 transparent, or light brownish with a size range of 30–250 μm × 30–125 μm and length-width
343 ratios ranging from 5:1 and 1:1. Most zircon crystals have subhedral to euhedral habits and

show mainly prismatic morphologies. Sub-rounded shapes are a common feature in some zircons, as well as stumpy morphologies. In general, the internal structure of the zircons varies between oscillatory zoning and core-rimmed patterns. The detrital cores display weakly oscillatory zoning, patchy zoning and simple broad zoning and are wrapped by dark-colored overgrowth rims (Figure 8A).

A total of seventy-nine spots were analyzed on 69 zircons from sample 10029. Seventy-three spots (73) yielded ages with concordance > 90% (Appendix Table 4), including 18 analyses on metamorphic overgrowth rims and 55 analyses on inherited cores. Th/U ratios in the range of 0.01 to 0.22 for the 18 overgrowth rim spots agree with a metamorphic origin for the zircons (Rubatto, 2017). These 18 overgrowth rims produced six concordant spots with an upper intercept age of 2106 ± 9.5 Ma (MSWD = 4), a $^{207}Pb/^{206}Pb$ weighted mean age of 2099 ± 6 Ma (MSWD = 2.19) and the youngest remnants a lead-loss trend line (Figure 8D). This dataset is interpreted to likely represent a metamorphic tectonothermal event, giving a minimum constraint for the depositional age of the sedimentary protolith.

The assumed maximum sedimentation age for the protolith corresponds only to the concordant zircons older than the metamorphism previously identified at ca. 2099 Ma and its anchored lead-loss trending line. This approach followed Spencer et al., (2016) criteria for defining maximum depositional ages. Therefore, the youngest population, given by 14 zircons, excluding the metamorphic crystals, resulted in a weighted mean $^{207}Pb/^{206}Pb$ age of 2152 Ma (Figure 8E).

5. Discussion

5.1. Provenance, detrital contribution and post-depositional features from the manganese-bearing rocks

Because the mineral assemblage of the manganese-bearing rocks from the Borborema Province is mainly composed of calc-silicate minerals (e.g., garnet, pyroxene, and minor carbonate), primary silicic marlstones or likely a silicate-rich chemical precursor are considered a potential protolith for the manganese-rich rocks. Thus, a first hypothesis is that the mineral phases precursors are believed to be kutnohorite-like carbonate minerals (Johnson et al., 2016; Santos et al., 2021). In the present study, this assumption comes from a textural relationship where kutnohorite-like carbonate occurs as inclusions in the garnet-spessartine crystals and manganese-pyroxene, suggesting a pre-metamorphic precipitation (Johnson et al., 2016; Polgári et al., 2012; Santos et al., 2021). After that, metamorphic spessartine garnet and manganese pyroxene minerals would develop by isochemical decarbonation and dehydration

reactions during prograde metamorphism, according to the following reactions:

$3MnCO_{3\ (Rhodochrosite\ or\ kutnohorite)} + Al_2Si_4O_{10}(OH)_{2\ (clay)} = Mn_3Al_2(Si_3O_{12})_{(Spessartine)} + SiO_{2\ (Quartz)} + H_2O + 3CO_2$ (1)

$3MnCO_{3\ (Rhodochrosite\ or\ kutnohorite)} + SiO_{2\ (Quartz)} + Al_2Si_2O_5(OH)_{4\ (clay)} = Mn_3Al_2(Si_3O_{12})_{(Spessartine)} + 2H_2O + 3CO_2$ (2)

$MnCO_{3\ (Rhodochrosite)} + SiO_{2\ (Quartz)} = MnSiO_{3\ (Rhodonite)} + CO_2$ (3),

The fact that all manganese phases contain Mn^{2+} oxidation state (e.g., $Mn_3^{2+}Al_2(Si_3O_{12})_{Spessartine}$ and $Mn^{2+}(SiO_3)_{Rhodonite}$), which reflect diagenesis and metamorphism of an early-reduced Mn precursor, like Mn-carbonate, further supported our view. Alternatively, assuming that some of these silicates may have had a volcanic-exhalative origin (e.g., spessartite and rhodonite; see Spry et al., 2000), it is also possible that the listed above mineral assemblages may have fully developed chemically, producing a marl-like composition. This approach suggests that SiO_2, clay minerals, and $MnCO_3$ were formed authigenically rather than derived from detritus, explaining the low Ti values found in these rocks (Figure 4 and Appendix Table 1). In all manganese-bearing rocks, Al_2O_3 and TiO_2 displayed negative correlations with MnO concentrations, indicating that terrigenous components were not the dominant source of the manganese-bearing rocks (Figures 4 and 5). Conversely, once Ti is a good detrital proxy, the very low TiO_2 (Appendix Table 1) values found in all manganese-bearing rocks support an absence of a detrital source or, at least, a Ti-poor source at the provenance of the manganese-bearing rocks. Also, Th and Sc yielded values lower than crustal average, with some samples showing detectable depletion (EF < 1).

Working with the alternative hypothesis where these rocks were pure chemical precipitates, then the SiO_2 combined with diagenetic Mn carbonate (according to reactions below) to produce manganese-rich silicates may have been an authigenic product of a seafloor dissolved silicic acid delivered from a submarine basaltic weathering. Such fluids would have been acidic and therefore limited the precipitation of carbonates, which is consistent with the low carbonate content of these rocks. This association is also supported by the relationship between Al and Ti values found. For example, 20-30% of Al is authigenic (clay minerals) in the deep open ocean, while Ti is rarely authigenic (Wei et al., 2003). Thus, the low Ti values found in these manganese-bearing rocks are consistent with the lack of a detrital influence and

412 a Ti-poor source, suggesting a chemical origin. The likely leached mafic/ultramafic source
413 rocks show low-Ti values (Appendix Table 1). A basic magmatic provenance is further
414 supported by the A-CN-K and Th/Sc *vs* Zr/Sc diagrams (Fedo et al. 1995; Nesbitt, 2003;),
415 which indicates that the manganese-rich silicates follow weathering trend of basalts (Figures
416 9a and b). Conversely, weathering of continental crust rocks should follow the sediment
417 recycling trend, becoming rich in Zr content. However, Zr is not enriched in samples relative
418 to UCC.
419 Although basaltic rocks are not associated with the drill cores, further south of the
420 present study area, several volcanic mafic bodies with ages ranging from outcrops of 2.2-2.1
421 Ga mafic bodies in contact with manganese silicate rocks (Martins et al., 2009; Costa et al.,
422 2015; Sousa et al., 2019; Appendix Table 1). The age range of these mafic rocks overlaps with
423 the inferred depositional age of the manganese-bearing rocks in this study. It is believed that
424 such mafic rocks were deposited as oceanic plateau basalts close to 2.2 Ga (Martins et al.,
425 2009). The concentrations of Ni, V and Co of up to 920 ppm, 350 ppm and 90 ppm, respectively
426 in these basaltic rocks (Martins et al., 2009; Sousa et al., 2019), as well as negative Eu
427 anomalies, are comparable with those recorded in the Mn-rich samples, which makes them
428 potential candidate source rocks. Thus, the incorporation of the reduced Mn^{2+} into early bottom
429 silicates that harbor a negative Eu anomaly, high Co, Ni, As and V concentrations may be
430 related to Mn leaching of a seafloor basaltic source. Because such negative Eu anomalies in
431 basalts reflect crystallization from magmas depleted by the precipitation of plagioclase-rich
432 rocks in the magma crystallization series, it could also mean that Mn was leached from such
433 magmas in contact with seawater into the sedimentary pile. Furthermore, basaltic volcanism as
434 a metal source is also a common feature in the Phanerozoic as showed by carbonate sediments
435 from the proto-North Atlantic deposited during the oceanic anoxic event 2 (OAE-2; Orth et al.,
436 1993).
437 The systematic negative to low positive Eu anomalies (0.38-1.27) in our rock samples
438 suggests that high-temperature hydrothermal processes did not contribute significantly to the
439 manganese precipitation since positive Eu anomalies are a diagnostic feature of high-
440 temperature hydrothermal fluids (>250ºC; e.g., Derry and Jacobsen, 1990; Douville et al.,
441 1999; German and Von Damm, 2003; Frei et al., 2017; Schier et al., 2020). Considering the
442 paleogeography and the distribution of mafic rocks in the Northern Borborema Province, the
443 distal deposition of manganese-rich rocks from the hydrothermal source might explain the
444 diminished intensity of the positive Eu anomaly (Steadman and Spry, 2015). Other possibilities
445 are Eu anomalies imprint by submarine weathering of a fractionated oceanic basaltic source

446 (Towell et al., 1969; Menzias et al., 1977; Rudnick, 1992) as suggested previously or lower
447 temperature hydrothermal fluids (e.g., Schier et al., 2020). The Ongeluk jaspilites (Hotazel
448 Formation, South Africa) is an example of a chemical precipitate lacking positive Eu anomaly
449 due to mixing of low-T hydrothermal fluids (<200ºC) with ambient seawater (Gutzmer et al.,
450 2001; Schier et al., 2020). Furthermore, it is also possible that the loss of positive Eu anomaly
451 may have been prompted by some detrital dilution of the seawater chemical components.
452 However, as true cerium anomalies are recorded in the manganese-bearing rocks and the TiO_2
453 is very low, diluting by terrigenous components may be unlikely.
454 Regardless, the trace and major element data, EFs and comparisons to the UCC, linked
455 to Eu anomalies, strongly oppose a detrital or pure hydrothermal source for the deposit. Instead,
456 the positive correlation between Co, V, As, and sedimentary Mn content in the manganese-rich
457 silicates, in the absence of a similar correlation with Cr, abundant in oxygenated seawater due
458 to oxidative weathering from continental rocks, suggest a non-UCC provenance (Figure 9a and
459 b). Furthermore, because Mn, As, Ni, Co and V, are strongly enriched in the manganese-rich
460 silicates, with much weaker patterns in the manganese-poor silicates (Figure 3; Appendix Table
461 3), a distinct provenance between these two lithologies may be taken into account. A basaltic
462 source is suggested for the Mn-rich rocks, whereas in the Mn-poor lithologies, a mixed-source
463 with some degree of detrital influence cannot be ruled out. Additionally, the strong positive
464 correlation between Co and V and MnO suggests the Mn-rich fluids were likely enriched in Co
465 and V. Similarly, the Mn-precipitating fluids are suggested to have been relatively depleted in
466 As, Ni, and as depicted by their strong enrichment factors but only moderate correlation with
467 MnO (Figure 5). However, another possibility to explain these moderate correlations is related
468 to a potential metamorphic redistribution of As and Ni in the rock. In this scenario, these
469 elements initially were deposited along with Mn and due to later diagenetic and metamorphic
470 processes, and then they were bound into other newly nucleated minerals. The data also suggest
471 that the fluids that combined to precipitate the Mn-rich rocks were generally depleted in Cu
472 and Cr, as depicted by weak enrichment factors and the extremely weak or inverse correlations
473 with the precipitated MnO.
474 Based on the above consideration, it is assumed that the reported redox signatures are
475 robust, in agreement with several studies that have used similar arguments to extract
476 paleoenvironment signals from late-diagenetic rocks and greenschist to amphibolite facies
477 sequences (e.g., Bolhar et al., 2004; Frei et al., 2017; Tashiro et al., 2017; Teixeira et al., 2017a;
478 Planavsky et al., 2018; Hood et al., 2018; Liu et al., 2019; Pitarello et al 2019; Cabral et al.,
479 2019b; Bosco-Santos et al., 2020; Zhang et al., 2020).

480

481 **5.2. Origin and paleoredox depositional conditions of the Mn-bearing rocks: Insights**
482 **from trace element and REE systematics**

483 The authigenic nature of some paleo-redox trace metals and metalloids (e.g., As, Co,
484 Cu, Mn, Mo, Ni; see Figure 3) may suggest that the manganese-bearing rocks from this study
485 were precipitated from a metal-rich, volcanically derived, seawater (Little et al., 2015). Co-
486 precipitation of sulfide minerals (Mo, As, Cu), passive scavenging of Mo, Ni, and Cu by a
487 particulate shuttle and the benthic Fe-Mn redox shuttle are secondary mechanisms potentially
488 responsible for transferring these metals to the rocks. In support of this view, all lithological
489 groups presented here contain sulfide minerals likely formed during the pre-metamorphic
490 stages of diagenesis and only recrystallized during metamorphism. For example, sedimentary
491 textural relationship demonstrated by cobaltite (CoAsS) and surrounding matrix minerals in
492 triple contact at approximately 120º, suggest early mineral growth can occur without reacting
493 with neighboring minerals (e.g., Cabral et al., 2019a). According to this feature, cobaltite either
494 was crystallized during early diagenesis as an authigenic precursor of an As-S-bearing
495 sedimentary rock or recrystallized during metamorphism. Furthermore, a previous volcanic
496 activity in the manganese source area (e.g., Martins et al., 2009; Costa et al., 2015; Sousa et
497 al., 2019), as discussed in the previous section, provides a reasonable explanation for the high
498 As enrichment in the samples. For example, a sample from the SMR group (#10243) showed
499 As concentrations of 978 ppm with an EF of 1542, comparable in magnitude to those achieved
500 by Archean and Paleoproterozoic Mn-Fe-rich sequences (Chi Fru et al., 2019).

501 Covariance between U and Mo is observed and speculated to be related to an Mn-oxide
502 particulate shuttle mechanism. However, U is unaffected in this process, remaining within
503 concentrations close to the crustal average (Algeo and Tribovillard, 2009; Wu et al., 2016; Ma
504 et al., 2019). Interestingly, the U enrichment factor detected in our Mn-bearing rocks is only
505 slightly above crustal levels (EF up to 3), supporting the statement above. The Mo_{EF} *versus* U_{EF}
506 plot (Figure 10) according to Algeo and Tribovillard (2009), reveals pronounced Mo
507 enrichment of up to 360 relatives to a maximum of 2.8 for U, providing additional support for
508 oxide shuttling from surface oxic to euxinic bottom sediments, similar to observations in the
509 modern weakly restricted and stratified Cariaco and the Baltic Sea basins (Algeo and
510 Tribovillard, 2009; Van Helmond et al., 2018). Normally Mn oxide shuttling to anoxic or
511 eventually euxinic waters results in high Mo enrichment in the bottom sediments (Algeo and
512 Tribovillard, 2009). Such high Mo EF is found in the manganese-rich silicate rocks (EF= 20 to
513 360), which is believed to have been deposited in an anoxic/euxinic setting according to Santos

et al. (2021). The ubiquitous dissemination of sulfide minerals (e.g., cobaltite and pyrite), as well as biogenic graphite (pyrolyzed remnants of organic matter; Fragomeni and Pereira, 2013) in these manganese-rich rocks, supports this interpretation. Thus, the high Mo enrichment in the Mn-rich rocks indicates simultaneous scavenging of seawater Mo and Mn from the oxic surface waters by Mn oxyhydroxides following a reductive dissolution mechanism of the Mn oxyhydroxides in the anoxic seafloor below the chemocline and later incorporation into the diagenetic-metamorphic Mn silicates. However, these results cannot fully differentiate between anoxic bottom waters and anoxic pore waters.

Besides the stated above, in anoxic/euxinic bottom sediments, Mn usually can react with carbonates to form authigenic Mn-carbonate minerals (e.g., kutnohorite and rhodochrosite; Calvert and Pedersen, 1993, 1996; Brumsack, 2006; Tribovillard et al., 2006; Johnson et al., 2016). Following this approach and according to other authoritative sources (De Putter et al., 2018; Chisonga et al., 2012; Cabral et al., 2019b; Mücke et al., 1999; Slack et al., 2000; Mancini et al., 2000; Nyame, 2001), it is suggested that the manganese-silicates (e.g., spessartine and rhodonite) may represent diagenetic/metamorphic products of authigenic silicates plus manganese-carbonate minerals reduced in the deep anoxic/euxinic seawater from Mn oxides precipitated above the chemocline. Support for this also comes from the strong true positive Ce anomaly (e.g., Warke et al. 2020).

To varying degrees, trace metals and metalloids such as V, Co, As and Ni, exhibit a reasonable covariance with Mn concentrations. Specifically, the reduction of vanadate to vanadyl ions (VO^{2-}) as well as hydroxyl forms, occur in mildly reducing and non-sulfidic anoxic waters (Algeo and Maynard, 2004; Calvert and Pedersen, 1993; Morford and Emerson 1999; Tribovillard et al., 2006; Gambacorta et al., 2020). Additionally, V^{3+} phases are further reduced to insoluble hydroxide forms under strongly reducing conditions when free H_2S is present in the euxinic environment (Tribovillard et al., 2006; Takahashi et al., 2014; Zhang et al., 2019). Since potential authigenic sulfide phases (e.g., pyrite and cobaltite) are mineralogically related to manganese minerals, most samples plot in the euxinic field on the Mo_{EF} *versus* U_{EF} graph, we suggest strongly reducing local conditions were associated with deposition of the Mn-protolith. Algeo and Maynard (2004) highlight that Cr is depleted in euxinic environments due to organic matter degradation by the action of sulfate-reducing bacteria. Although we do not have direct evidence for sulfate reduction, the co-occurrence of pyrite with graphitic lenses, coupled to the low Cr enrichment factor (Figure 3) and a lack of covariation between Cr and Mn (Figure 5), suggest a strong possibility for microbial sulfate to sulfide reduction with organic matter in low oxygen waters below the Mn-chemocline.

548 The proposition of euxinic bottom waters is reinforced by As cycling. Under oxidizing
549 waters, As^{5+} may be incorporated into Mn-oxyhydroxides reactive surfaces, forming insoluble
550 arsenic forms (Tribovillard, 2020). While under reducing conditions, As^{5+} is reduced to As^{3+}
551 and may react with sulfide species precipitated in euxinic bottom sediments (e.g., Morse and
552 Luther, 1999; Huerta-Diaz and Morse, 1992; An et al., 2017; Hetzel et al., 2011; Tribovillard,
553 2020). Consequently, the reductive dissolution of Mn oxides across the chemocline would have
554 released As^{5+} into the seawater, which would have been reduced to As^{3+} and incorporated into
555 sulfide minerals forming in the water column and on the seafloor. The high As enrichment
556 factor in our samples and the moderate positive covariance with Mn concentrations suggest
557 this shift towards As enrichment in the anoxic/euxinic conditions existing beneath the
558 chemocline. As the positive relationship between As and MnO enrichments accounts for only
559 40% of the data, As is suggested to have had a likely seawater surface and an association with
560 the basaltic weathering fluids.
561 Cerium anomaly is an oxygen sensitive proxy widely used to unravel ocean water column
562 redox (Elderfield et al., 1988; Liu et al., 1988; German and Elderfield, 1990; Shields and Stille
563 2001). In anoxic waters, Ce^{3+} is soluble but oxidizes to Ce^{4+} in oxic (<5 µmol German and
564 Elderfield, 1990) near-neutral pH environments (Elderfield et al., 1988; German and Elderfield,
565 1990). When oxygen concentrations rise above 5 µmol, the oxidation of Ce^{3+} to Ce^{4+} lowers
566 the solubility of Ce, leading to its precipitation and depletion from seawater (Elderfield et al.,
567 1988; Liu et al., 1988). The removal of Ce^{4+} from seawater is enhanced by Mn-Fe
568 oxyhydroxides minerals, clay particles, and organic matter-rich deposits, which serve as
569 templates for Ce precipitation and deposition on the seafloor (Bau, 1999; Bau and Koschinsky,
570 2009; Tostevin et al., 2016a). This depletion in seawater Ce concentration linked to negative
571 Ce anomalies recorded in the water column is consistent with the concomitant dependence of
572 Mn^{2+} oxidization to $Mn^{3+/4+}$ on oxygen availability **(**Calvert and Pedersen, 1996; Post, 1999;
573 Tebo et al., 2005; Johnson, 2015**)**. Negative Ce anomalies can also develop during oxidative
574 weathering of continental rocks, resulting in the discharge of Ce-depleted riverine waters into
575 the ocean (Frei et al., 2017).
576 In general, three manganese-bearing samples yielded true negative cerium anomalies,
577 which reflect deposition from oxic seawater (Figure 7). Conversely, positive Ce anomalies
578 were recorded in seven manganese-bearing samples, six from manganese-rich silicates and one
579 from the manganese-poor group (see Figure 7). Positive Ce anomaly is a reliable proxy for
580 redox-stratified basins because the reductive dissolution of Mn-oxyhydroxides particles to
581 soluble Mn^{2+} across a redoxcline drives seawater Ce enrichment (e.g., Warke et al., 2020). In

582 our case, this would indicate the existence of a chemocline in the seawater, dividing an upper
583 oxidized zone from a lower anoxic zone (Figure 11). Thus, the reductive release of Ce^{4+}
584 precipitated from the overlying oxic zone to Ce^{3+} in the anoxic zone below the chemocline
585 results in anomalous Ce enrichment to explain the positive anomalies, leading to the transfer
586 of Ce and reduced Mn^{2+} to anoxic bottom sediments (Planavsky et al., 2010; Tostevin et al.,
587 2016b; Warke et al., 2020). Such a scenario results in Mn-oxide shuttle from oxic surface
588 waters to the deep anoxic sediment-water interface (Dellwig et al., 2010; Planavsky et al.,
589 2010; Tostevin et al., 2016b). Furthermore, manganese-(oxy)hydroxide minerals may re-
590 precipitate during oxic events, likely on a regressive setting when chemocline shifts downward.
591 Overall, this relationship agrees with the assumption that high authigenic Mo enrichment took
592 place in anoxic/euxinic bottom carbonaceous sediments by the reductive dissolution of
593 Mn(oxy)hydroxides particles.
594 The observed fractionations between LREE to HREE ratios (e.g., Sm_{SN}/Yb_{SN}
595 variations), mainly in the manganese-rich silicates, indicate a slight LREE depletion compared
596 to MREE and HREE. This further suggests the existence of an Mn-chemocline because LREE
597 is expected to be scavenged by Mn oxyhydroxides precipitated from oxic zones, leading to
598 REE fractionation (Byrne and Sholkovitz, 1996; Bau et al., 1997; Planavsky et al., 2010). The
599 fractionation range between REE ratios is a common feature of modern and ancient redox-
600 stratified basins, contrasting from the early Paleoproterozoic basins characterized by a
601 predominantly LREE depletion pattern (Planavsky et al., 2010). However, the possibility that
602 LREE depletions are not systematically well characterized in our samples may indicate
603 proximity to the Mn-chemocline (Planavsky et al., 2010). In many redox-stratified
604 environments, the LREE to HREE ratios has shale-like patterns close to the Mn-
605 redoxcline (Planavsky et al., 2010). The REE pattern from the manganese-poor rocks is similar
606 to the average-shale composition pattern, suggesting their deposition across an Mn-
607 redoxcline. Alternatively, another possibility for this pattern is that some REE dilution may
608 have occurred by the influence of minor terrigenous components or alternatively by authigenic
609 clays.
610 Furthermore, the preservation of positive Ce signals in our metamorphosed manganese
611 rocks is in agreement that diagenesis and metamorphism have not interfered with the REEs
612 arrays and anomalies, possibly because these reactions were isochemical (e.g., Bau, 1991;
613 Cabral and Moore., 2012; Planavsky et al., 2018; Grenne and Slack, 2019; Cabral et al., 2019b;
614 Wark et al., 2020). Strikingly, the Ce patterns and Ce_{SN}/Ce_{SN}* *versus* Pr_{SN}/Pr_{SN}* anomalies are
615 similar to those recorded in the 1.9 Ga Biwabik Iron Formation, Lake Superior region

precipitated from a redox-stratified ocean (Planavsky et al., 2010).

5.3. Implications for Paleoproterozoic seawater-atmosphere oxygenation

In the context of South America and Africa, the data suggest an association with the Transzamazonian and Eburnean orogenesis (Alkmim and Marshak, 1998; Rosa-Costa et al., 2006; Feybesse et al. 2006; Vasquez et al. 2008; Brito Neves., 2011; Baratoux et al., 2011; Teixeira et al., 2017b). It is suggested that these events were most probably responsible for the metamorphic fingerprints recorded in the rocks, similar to events in the Francevillian manganese deposits in the Congo craton. It has previously been shown that manganese-bearing rocks, both from South America and Northwest Africa, have experienced varying degrees of metamorphism (Klein and Moura, 2008; Neves, 2011; Costa et al., 2018; Grenholm, 2019 Grenholm et al., 2019), which may reflect the interaction of tectonic plates during the closing of ancient oceanic basins. Globally, the studied rocks are associated with an interval characterized by the agglutination of the so-called Columbia supercontinent, suggested to be related to triggering the metamorphism of the manganese precursors at this time (Roy, 2006; Maynard, 2010; Johnson et al., 2016).

A standard view state that manganese requires an electron receptor with high redox potential, such as oxygen, for oxidation (Calvert and Pedersen, 1996; Post, 1999; Tebo et al., 2005; Johnson, 2015). Additionally, O_2-free mechanisms can also be invoked for manganese precipitation (e.g., Johnson et al., 2013; Daye et al., 2019; Anbar and Holland, 1992, Liu et al., 2020). Nevertheless, as the manganese-bearing rocks from this study were deposited during the permanent rise of oxygen in the oceans and atmosphere (~2.22 Ga), it is likely that they were also affected by it, excluding an anoxygenic mechanism on the manganese deposition in a first approach. Although the oceanic and atmospheric oxygenation conditions in the aftermath of the Great Oxidation Event during the Lomagundi Jatuli-Event (e.g., 2.21-2.06 Ga.; Bekker et al., 2006; Melezhik et al., 2007; Kump et al., 2011; Bekker and Holland, 2012; Bekker, 2014) are still a matter of debated. While some workers point to a period of deoxygenation, others to oxygenated conditions (Bekker and Holland, 2012; Canfield et al., 2013; Asael et al., 2018; Ossa Ossa et al., 2018; Kump et al., 2011; Kreitsmann et al., 2020; Mänd et al., 2020). For example, in the ca. 2.1 Ga Franceville Group, Gabon, well-oxygenated shallow waters may have given way to stratified waters characterized by deep manganous/ferruginous waters separated waters from predominantly oxic surface ocean waters by a redoxcline (e.g., Canfield et al., 2013; Ossa Ossa et al., 2018; Mayika et al., 2020). Similar conditions have been reported for the Late Paleoproterozoic Animikie Basin (Planavsky et al., 2018). On the other hand, the

chemical record from the rocks in the Onega Basin, specifically in the Zaonega Formation, indicates predominantly oxygenated shallow water conditions in the aftermath of the GOE (Paiste et al., 2018; Kreitsmann et al., 2020; Mänd et al., 2020). These clues suggest that this period marked a transitional phase between the anoxic Archean ocean-atmosphere and the fully oxic modern ocean-atmosphere system. But overall, there is strong consensus that oxygenic photosynthesis played a significant role in this crucial environmental change (Canfield et al., 2013; Bekker, 2014; Lyons et al., 2014). Our finds agree with some of these works by pointing out a redox-stratified setting where manganese-bearing minerals precipitate and add a new sink (e.g., chemical silicates) in the manganese cycling.

6. Conclusion

Collective analysis of REEs and redox-sensitive trace metals in manganese-rich rocks from the Borborema Province in northeast Brazil, coupled to U-Pb geochronology, suggest a depositional pathway for ore grade manganese formation in the Paleoproterozoic Borborema basin. With a reconstructed age of 2.2-1.9 billion years ago, this study points to large-scale weathering and leaching of seafloor basaltic rocks or basaltic magmas in contact with seawater as the source of Paleoproterozoic manganese enrichment. The oxidation and shuttling of reduced Mn as Mn-oxide from oxic surface waters and subsequent reduction across the chemocline produced deep seafloor Mn deposits primarily associated with manganese silicate and carbonate minerals. This contribution adds to a growing body of work pointing to global seawater redox stratification during the Paleoproterozoic, linked to local seawater chemistry, mineralogy and basin-scale tectonic and sedimentary conditions.

Acknowledgments

The first author is grateful to the Federal University of Western Pará (UFOPA) for support throughout the time, and to the Geologist Renato Braz Sue (on behalf of Libra Ligas do Brasil company) for providing full access to drill cores and fieldwork assistance. FHS would like to thank the Society of Economic Geologists for the Student Research Grant received. This research is part of the first author's Ph.D. thesis. We truly appreciate the comments, suggestions and criticisms from Leslie Robbins, Eva Stüeken and two anonymous reviewers that helped to improve the quality of this manuscript. In addition, we also thank the editorial handling by Professor Michael E. Böttcher. WSA also acknowledges the Brazilian National Research Council (CNPq) for research grant (process. 305263/2020-0) and the Cardiff University.

683

684 **References**

685 Albarède, F. (2005) The survival of mantle geochemical heterogeneities. In van der Hilst, R.,
686 et al., eds, Structure, Composition, and Evolution of Earth's Mantle. Geophysical Monograph
687 of the American Geophysical Union 160, 27–46.
688
689 Algeo T. J. and Tribovillard N. (2009) Environmental analysis of paleoceanographic systems
690 based on molybdenum–uranium covariation. Chem. Geol. 268(3), 211–225.

691 Algeo, T.J., Li, C., 2020. Redox classification and calibration of redox thresholds in
692 sedimentary systems. Geochim. Cosmochim. Acta 287, 8–26.

693 Algeo, T.J., Maynard, J.B., 2004. Trace-element behavior and redox facies in core shales of
694 Upper Pennsylvanian Kansas-type cyclothems. Chem. Geol. 206, 289–318.

695 Alkmim, F.F., Marshak, S., 1998. Transamazonian Orogeny in the Southern São Francisco
696 Craton Region, Minas Gerais, Brazil: Evidence for Paleoproterozoic collision and collapse in
697 the Quadrilátero Ferrífero. Precambrian Res. 90, 29–58.

698 An, X.L., Huang, F.G., Rend, H.T., Wang, Y.F., Chen, Y., Liu, Z.M., Zhang, H.W., 2017.
699 Oxidative dissolution of amorphous FeS and speciation of secondary Fe minerals: effects of
700 pH and As (III) concentration. Chem. Geol. 462, 44–54.

701 Anbar, A.D., Holland, H.D., 1992. The photochemistry of manganese and the origin of banded
702 iron formations. Geochim. Cosmochim. Acta 56, 2595–2603.

703 Asael, D., Rouxel, O., Poulton, S.W., Lyons, T.W., Bekker, A., 2018. Molybdenum record
704 from black shales indicates oscillating atmospheric oxygen levels in the early Paleoproterozoic.
705 Am. J. Sci. 318, 275–299.

706 Baratoux, L., Metelka, V., Naba, S., Jessell, M.W., Grégoire, M., Ganne, J., 2011. Juvenile
707 Paleoproterozoic crust evolution during the Eburnean orogeny (~2.2-2.0Ga), western Burkina
708 Faso. Precambrian Res. 191, 18–45.

709 Bau, M., 1999. Scavenging of dissolved yttrium and rare earths by precipitating iron
710 oxyhydroxide: experimental evidence for Ce oxidation, Y–Ho fractionation, and lanthanide
711 tetrad effect. Geochim. Cosmochim. Acta 63, 67–77.

712 Bau, M., Alexander, B., 2006. Preservation of primary REE patterns without Ce anomaly
713 during dolomitization of Mid-Paleoproterozoic limestone and the potential reestablishment of
714 marine anoxia immediately after the "Great Oxidation Event". South Afr. J. Geol. 109, 81–86.

715 Bau, M., Dulski, P., 1996. Distribution of yttrium and rare-earth elements in the Penge and
716 Kuruman iron-formations, Transvaal Supergroup, South Africa. Precambr. Res. 79 (1–2), 37–
717 55.

718 Bau, M., Koschinsky, A., 2009. Oxidative scavenging of cerium on hydrous Fe oxide: evidence
719 from the distribution of rare earth elements and yttrium between Fe oxides and Mn oxides in
720 hydrogenetic ferromanganese crusts. Geochem. J. 43, 37–47.

721 Bau, M., Möller, P., Dulski, P., 1997. Yttrium and lanthanides in eastern Mediterranean
722 seawater and their fractionation during redox cycling. Mar. Chem. 56, 123–131.

Bau, M., Schmidt, K., Koschinsky, A., Hein, J., Kuhn, T., Usui, A., 2014. Discriminating between different genetic types of marine ferro-manganese crusts and nodules based on rare earth elements and yttrium. Chem. Geol. 381, 1–9.

Bekker A., Karhu, J.A., Kaufman, A.J., 2006. Carbon isotope record for the onset of the Lomagundi carbon isotope excursion in the Great Lakes area, North America. Precambrian Res 148:145–180.

Bekker, A., 2014. Lomagundi carbon isotope excursion. In: Encyclopedia of Astrobiology. Springer-Verlag, pp. 1–6.

Bekker, A., Holland, H.D., 2012. Oxygen overshoot and recovery during the early Paleoproterozoic. Earth Planet. Sci. Lett. 317–318, 295–304.

Beukes, N.J., Swindell, E.P.W., Wabo, H., 2016. Manganese deposits of Africa. Episodes 39, 285–317.

Bolhar, R., Kamber, B.S., Moorbath, S., Fedo, C.M., Whitehouse, M.J., 2004. Characterisation of early Archaean chemical sediments by trace element signatures. Earth Planet. Sci. Lett. 222, 43–60.

Bosco-Santos, A., Gilhooly, W.P., Fouskas, F., Fabricio-Silva, W., Oliveira, E.P., 2020. Euxinia in the Neoarchean: The starting point for early oxygenation in a Brazilian Craton. Precambrian Res. 341, 105655.

Brito Neves, B.B., 2011. The Paleoproterozoic in the South American continent: Diversity in the geologic time. J. South Am. Earth Sci. 32, 270–286.

Brito Neves, B.B., Santos, E.J., and Van Schmus, W.R., 2000, in Tectonic History of the Borborema Province, Northeast Brazil, Cordani, U.G., Milani, E.J., Thomaz Filho, A., and Campos, D.A., Eds., Tectonic Evolution of South America, Rio de Janeiro, 31st International Geological Congress, p. 151–182.

Brumsack, H.J., 2006. The trace metal content of recent organic carbon-rich sediments: implications for Cretaceous black shale formation. Palaeogeography Palaeoclimatology Palaeoecology 232, 344–361.

Byrne R. and Sholkovitz E. (1996) Marine chemistry and geochemistry of the lanthanides. In Handbook on the Physics and Chemistry of the Rare Earths (eds. K. A. Gschneider Jr. and L. Eyring). Elsevier, Amsterdam.

Cabral, A. R., & Moore, J. M. (2012). Negative cerium anomaly in spessartine garnet from a barite-rich rock, Otjosondu ferromanganese deposit, Namibia: the fingerprint of oxic sea water. South African Journal of Geology, 115(4), 589-596.

Cabral, A.R., Zeh, A., Viana, N.C. da S., de Castro, M.P., Laufek, F., Lehmann, B., Queiroga, G., 2019a. Alabandite (MnS) in metamorphosed manganiferous rocks at Morro da Mina, Brazil: palaeoenvironmental significance. Eur. J. Mineral. 31, 973–982.

Cabral, A.R., Zeh, A., Vianna, N.C., Ackerman, L., Pašava, J., Lehmann, B., Chrastný, V., 2019b. Molybdenum-isotope signals and cerium anomalies in Palaeoproterozoic manganese ore survive high-grade metamorphism. Sci. Rep. 9, 1–7.

762 Caby, R., 1989. Precambrian terranes of the Benin-Nigeria and Northeast Brazil and the late
763 Proterozoic South Atlantic fit: Geological Society of America Special Paper, v. 230, p. 145–
764 158.

765 Calado, B.O., Costa, F.G., Gomes, I.P., Rodrigues, J.B., 2019. Evidence for ca. 2046 Ma high-
766 grade metamorphism in Paleoproterozoic metasedimentary rocks of the northern Borborema
767 Province, NE Brazil: constraints from U-Pb (LA-ICP-MS) zircon ages. Journal of the
768 Geological Survey of Brazil, 2(3), 137-150.

769 Calvert, S.E., Pedersen, T.F., 1993. Geochemistry of recent oxic and anoxic marine sediments:
770 implications for the geological record. Mar. Geol. 113, 67–88.

771 Calvert, S.E., Pedersen, T.F., 1996. Sedimentary geochemistry of manganese: Implications for
772 the environment of formation of manganiferous black shales. Econ. Geol. 91, 36–47.

773 Canfield, D.E., 1998, A new model for Proterozoic ocean chemistry: Nature, v. 396, p. 450–
774 453.
775
776 Canfield, D.E., Poulton, S.W., Knoll, A.H., Narbonne, G.M., Ross, G., Goldberg, T., and
777 Strauss, H., 2008, Ferruginous conditions dominated later Neoproterozoic deep-water
778 chemistry: Science, v. 321, p. 949–952.
779
780 Canfield, D.E., Ngombi-Pemba, L., Hammarlund, E.U., Bengtson, S., Chaussidon, M.,
781 Gauthier-Lafaye, F., Meunier, A., Riboulleau, A., Rollion-Bard, C., Rouxel, O., Asael, D.,
782 Pierson-Wickmann, A.C., El Albani, A., 2013. Oxygen dynamics in the aftermath of the Great
783 Oxidation of Earth's atmosphere. Proc. Natl. Acad. Sci. U. S. A. 110, 16736–16741.

784 Castaing, C., Feybesse, J.L., Thiéblemont, D., Triboulet, C., Chèvremont, P., 1994.
785 Palaeogeographical reconstructions of the Pan-African/Brasiliano orogen: closure of an
786 oceanic domain or intracontinental convergence between major blocks? Precambrian Res. 69,
787 327–344.

788 Castro, N.A., 2004. Evolução Geológica Proterozoica da Região entre Madalena e Taperuaba,
789 Domínio Tectônico Ceará Central (Província Borborema). PhD Thesis. Instituto de
790 Geociências, USP, Sao Paulo-SP, p. 221.

791 Chi Fru, E., Arvestål, E., Callac, N., El Albani, A., Kilias, S., Argyraki, A., Jakobsson, M.,
792 2015. Arsenic stress after the Proterozoic glaciations. Sci. Rep. 5:17789. DOI:
793 10.1038/srep17789.

794 Chi Fru, E., Rodríguez, N.P., Partin, C.A., Lalonde, S.V., Andersson, P., Weiss, D.J., El
795 Albani, A., Rodushkin, I., Konhauser, K.O., 2016. Cu isotopes in marine black shales record
796 the Great Oxidation Event. Proc. Natl. Acad. Sci. U.S.A. 113:4941–4946.

797 Chi Fru, E., Somogyi, A., El Albani, A., Medjoubi, K., Aubineau, J., Robbins, L.J., Lalonde,
798 S. V., Konhauser, K.O., 2019. The rise of oxygen-driven arsenic cycling at ca. 2.48 Ga.
799 Geology 47, 243–246.

800 Chisonga, B.C., Gutzmer, J., Beukes, N.J., Huizenga, J.M., 2012. Nature and origin of the
801 protolith succession to the Paleoproterozoic Serra do Navio manganese deposit, Amapa
802 Province, Brazil. Ore Geol. Rev. 47, 59–76.

Chen, S.-C., Sun, G.-X., Yan, Y., Konstantinidis, K. T., Zhange, S.-Y., Denga, Y., Lia, X.-M., Cui, H. L. Musat, F., Popp, D., Rosen B. P., Zhu, Y.-G., 2020. The Great Oxidation Event expanded the genetic repertoire of arsenic metabolism and cycling. *Proceedings of the National Academy of Sciences*, *117*(19), 10414-10421.

Cordani, U.G., Ramos, V.A., Fraga, L.M., Cegarra, M.,Delgado, I., de Souza, K.G., Gomes, F.E.M., Schobbenhaus, C., 2016. Tectonic map of South America, 2th: Commission for the geological map of the world, scale 1:5.000.000, 1 sheet.

Costa F.G., Palheta E. 2017. Geologia e recursos minerais das folhas Quixadá (SB.24-V-B-IV) e Itapiúna (SB.24-X-A-IV). Escala 1:100.000. Fortaleza, CPRM. Available on line at: http://rigeo.cprm.gov.br/jspui/handle/doc/19029/

Costa, F.G., Klein, E.L., Lafon, J.M., Milhomem Neto, J.M., Galarza, M.A., Rodrigues, J.B., Naleto, J.L.C., Corrêa Lima, R.G., 2018. Geochemistry and U–Pb–Hf zircon data for plutonic rocks of the Troia Massif, Borborema Province, NE Brazil: Evidence for reworking of Archean and juvenile Paleoproterozoic crust during Rhyacian accretionary and collisional tectonics. Precambrian Res. 311, 167–194.

Costa, F.G., Palheta, E.S. de M., Rodrigues, J.B., Gomes, I.P., Vasconcelos, A.M., 2015. Geochemistry and U-Pb zircon ages of plutonic rocks from the Algodões granite-greenstone terrane, Troia Massif, northern Borborema Province, Brazil: Implications for Paleoproterozoic subduction-accretion processes. J. South Am. Earth Sci. 59, 45–68.

Dantas, E.L., De Souza, Z.S., Wernick, E., Hackspacher, P.C., Martin, H., Xiaodong, D., Li, J.W., 2013. Crustal growth in the 3.4-2.7Ga São José de Campestre Massif, Borborema Province, NE Brazil. Precambrian Res. 227, 120–156.

Daye, M., Klepac-Ceraj, V., Pajusalu, M., Rowland, S., Farrell-Sherman, A., Beukes, N., Tamura, N., Fournier, G., Bosak, T., 2019. Light-driven anaerobic microbial oxidation of manganese. Nature 576, 311–314.

De Putter, T., Liégeois, J.P., Dewaele, S., Cailteux, J., Boyce, A., Mees, F., 2018. Paleoproterozoic manganese and base metals deposits at Kisenge-Kamata (Katanga, D.R. Congo). Ore Geol. Rev. 96, 181–200.

De Wit, M.J., Brito Neves, B.B., Trouw, R.A.J., and Pankhurst, R. J., editors, 2008, West Gondwana: Pre-Cenozoic Correlations across the Atlantic Region, Volume 294: Geological Society of London, Special Publication, p. 1–8.

Dellwig, O., Leipe, T., März, C., Glockzin, M., Pollehne, F., Schnetger, B., Yakushev, E.V., Böttcher, M.E., Brumsack, H.J., 2010. A new particulate Mn–Fe–P-shuttle at the redoxcline of anoxic basins. Geochim. Cosmochim. Acta 74, 7100–7115.

Derry, L.A., Jacobsen, S.B., 1990. The chemical evolution of Precambrian seawater - Evidence from REEs in banded iron formations. Geochimica et Cosmochimica Acta 54, 2965-2977.

Douville E, Bienvenu P, Charlou JL, Donval JP, Fouquet Y, Appriou P, Gamo T (1999) Yttrium and rare earth elements in fluids from various deep-sea hydrothermal systems. Geochim Cosmochim Acta 63:627–643

842 Elderfield, H., 1988. The oceanic chemistry of the rare-earth elements. Philosophical
843 Transactions of the Royal Society of London Series a-Mathematical Physical and Engineering
844 Sciences 325, 105-126.

845 Farquhar, J., Bao, H., Thiemens, M., (2000). Atmospheric influence of Earth's earliest sulfur
846 cycle. Science 289, 756– 758.

847 Fedo, C.M., Nesbitt, H.W., and Young, G.M., 1995, Unraveling the effects of potassium
848 metasomatism in sedimentary rocks and paleosols, with implications for paleoweathering
849 conditions and provenance: Geology, v. 23, p. 921–924.

850 Fetter, A.H., 1999. U-Pb and Sm-Nd geochronological constraints on the crustal framework
851 and geologic history of Ceará State, NW Borborema Province, NE Brazil: Implications for the
852 assembly of Gondwana. Ph.D. Thesis, Kansas.

853 Fetter, A.H., Van Schmus, W.R., Santos, T.J.S., Nogueira Neto, J.A., Arthaud, M.H., 2000. U-
854 Pb and Sm-Nd Geochronological Constraints on the Crustal Evolution and Basement
855 Architecture of Ceará State, Nw Borborema Province, Ne Brazil: Implications for the Existence
856 of the Paleoproterozoic Supercontinent "Atlantica." Rev. Bras. Geociências 30, 102–106.

857 Feybesse, J.L., Billa, M., Guerrot, C., Duguey, E., Lescuyer, J.L., Milesi, J.P., Bouchot, V.,
858 2006. The paleoproterozoic Ghanaian province: Geodynamic model and ore controls,
859 including regional stress modeling. Precambrian Res. 149, 149–196.

860 Fragomeni, P.R.P., Pereira, R.M., 2013. The graphite mineralization in the Aracoiába-Baturité
861 District (CE): Geotectonic and metallogenetic implications. Brazilian J. Geol. 43, 223–234.

862 Frei, R., Døssing, L.N., Gaucher, C., Boggiani, P.C., Frei, K.M., Bech Árting, T., Crowe, S.A.,
863 Freitas, B.T., 2017. Extensive oxidative weathering in the aftermath of a late Neoproterozoic
864 glaciation – Evidence from trace element and chromium isotope records in the Urucum district
865 (Jacadigo Group) and Puga iron formations (Mato Grosso do Sul, Brazil). Gondwana Res. 49,
866 1–20.

867 Gambacorta, G., Bottini, C., Brumsack, H.J., Schnetger, B., Erba, E., 2020. Major and trace
868 element characterization of Oceanic Anoxic Event 1d (OAE 1d): Insight from the Umbria-
869 Marche Basin, central Italy. Chem. Geol. 557, 119834.

870 Ganade, C.E., Basei, M.A.S., Costa, F.G., Armstrong, R., Brito, R.S., 2017. Contrasting
871 Archaean (2.85–2.68 Ga) TTGs from the Tróia Massif (NE-Brazil) and their geodynamic
872 implications for flat to steep subduction transition. Precambrian Res. 297, 1–18.

873 Garcia M., Santos T., Amaral W. 2014. Provenance and tectonic setting of neoproterozoic
874 supracrustal rocks from the Ceará Central Domain, Borborema Province NE Brazil: constraints
875 from geochemistry and detrital zircon ages. Int. Geol. Rev. 56 (4), 1-20.

876 Gauthier-Lafaye, F., Weber, F., 2003. Natural nuclear fission reactors: time constraints for
877 occurrence, and their relation to uranium and manganese deposits and to the evolution of the
878 atmosphere. Precambrian Res.120, 81–100.

879 German CR, Von Damm KL (2003) Hydrothermal processes. In: Elderfield H (ed) The oceans
880 and marine geochemistry. Elsevier, Amsterdam. Treatise on Geochemistry 6:181–222

881 German, C.R., Elderfield, H., 1990. Application of the Ce-anomaly as a paleoredox indicator:
882 the ground rules. Paleoceanography 5, 823–833.

Gomes E.N. 2013. Protominérios e minérios de manganês de Juá-CE. MSc Dissertation, Instituto de Geociências, Universidade Federal do Ceará, Ceará, 102 p.

Grenholm, M., 2019. The global tectonic context of the ca. 2.27-1.96 Ga Birimian Orogen – Insights from comparative studies, with implications for supercontinent cycles. Earth-Science Rev. 193, 260–298.

Grenholm, M., Jessell, M., Thébaud, N., 2019. Paleoproterozoic volcano-sedimentary series in the ca. 2.27–1.96 Ga Birimian Orogen of the southeastern West African Craton. Precambrian Res. 328, 161–192.

Grenne, T., Slack, J.F., 2019. Mineralogy and geochemistry of silicate, sulfide, and oxide iron formations in Norway: evidence for fluctuating redox states of early Paleozoic marine basins. Miner. Depos. 54, 829–848.

Gumsley, A.P., Chamberlain, K.R., Bleeker, W., Söderlund, U., de Kock, M.O., Larsson, E.R., Bekker, A., (2017). Timing and tempo of the Great Oxidation Event. Proceedings of the National Academy of Sciences of the U.S.A. 114, 1811–1816.

Hetzel, H., März, C., Vogt, C., Brumsack, H.-J., 2011. Geochemical environment of Cenomanian - Turonian black shale deposition at Wunstorf (northern Germany). Cretac. Res. 32, 480–494.

Hodgskiss, M.S.W., Sperling, E.A., 2021. A prolonged, two-step oxygenation of Earth's early atmosphere: Support from confidence intervals. Geology XX, 1–5.

Holland, H.D., 2006. The oxygenation of the atmosphere and oceans. Philos. Trans. R. Soc. B Biol. Sci. 361, 903–915.

Hollanda, M.H.B.M., Archanjo, C.J., Souza, L.C., Dunyi, L., Armstrong, R., 2011. Long-lived Paleoproterozoic granitic magmatism in the Seridó-Jaguaribe domain, Borborema Province-NE Brazil. J. South Am. Earth Sci. 32, 287–300.

Hood, A.v.S., Planavsky, N.J., Wallace, M.W., Wang, X., 2018. The effects of diagenesis on geochemical paleoredox proxies in sedimentary carbonates. Geochim. Cosmochim. Acta 232, 265–287.

Huerta-Diaz, M.A., Morse, J.W., 1992. Pyritisation of trace metals in anoxic marine sediments. Geochim. Cosmochim. Acta 56, 2681–2702.

Javaux, E. J., & Lepot, K., 2018. The Paleoproterozoic fossil record: implications for the evolution of the biosphere during Earth's middle-age. Earth-Science Reviews, 176, 68-86.

Johnson, J. E., Webb, S. M., Thomas, K., Ono, S., Kirschvink, J. L., & Fischer, W. W. 2013. Manganese-oxidizing photosynthesis before the rise of cyanobacteria. Proceedings of the National Academy of Sciences, 110(28), 11238-11243.

Johnson, J.E., 2015. Manganese: Minerals, Microbes, and the Evolution of Oxygenic Photosynthesis. Dissertation (Ph.D.), California Institute of Technology.

Johnson, J.E., Webb, S.M., Ma, C., Fischer, W.W., 2016. Manganese mineralogy and diagenesis in the sedimentary rock record. Geochim. Cosmochim. Acta 173, 210–231.

Kah, L.C., Lyons T.W., Frank, T., 2004. Low marine sulphate and protracted oxygenation of the Proterozoic biosphere. Nature 431, 834–83

Karhu, J.A.; Holland, H.D., 1996. Carbon isotopes and the rise of atmospheric oxygen. Geology 24, 867–870.

Kirschvink, J.L., Gaidos, E.J., Bertani, W., Beukes, N.J., Gutzmer, J., Maepa, L.N., Steinberger, R.E., 2000. Paleoproterozoic snowball Earth: Extreme climatic and geochemical global change and its biological consequences. Proceedings of the National A. of Sciences of the United States of America, 15: 1400-1405.

Klein, E.L., Moura, C.A.V., 2008. São Luís Craton and Gurupi belt (Brazil): Possible links with the West African Craton and surrounding Pan-African belts. Geol. Soc. Spec. Publ. 294, 137–151.

Konhauser, K.O., Planavsky, N.J., Hardisty, D.S., Robbins, L.J., Warchola, T.J., Haugaard, R., Lalonde, S. V., Partin, C.A., Oonk, P.B.H., Tsikos, H., Lyons, T.W., Bekker, A., Johnson, C.M., 2017. Iron formations: A global record of Neoarchaean to Palaeoproterozoic environmental history. Earth-Science Rev. 172, 140–177.

Kreitsmann, T., Lepland, A., Bau, M., Prave, A., Paiste, K., Mänd, K., Sepp, H., Martma, T., Romashkin, A.E., Kirsimäe, K., 2020. Oxygenated conditions in the aftermath of the Lomagundi-Jatuli Event: The carbon isotope and rare earth element signatures of the Paleoproterozoic Zaonega Formation, Russia. Precambrian Res. 347, 105855.

Kuhn, T., Bau, M., Blum, N., Halbach, P., 1998. Origin of negative Ce anomalies in mixed hydrothermal-hydrogenetic Fe–Mn crusts from the Central Indian Ridge. Earth Planet. Sci. Lett. 163, 207–220.

Kump, L.R., Junium, C., Arthur, M.A., Brasier, A., Fallick, A., Melezhik, V., Lepland, A., Črne, A.E., Luo, G., 2011. Isotopic evidence for massive oxidation of organic matter following the great oxidation event. Science. 334, 1694–1696.

Leclerc, J., Weber, F., 1980. Geology and genesis of the Moanda manganese deposits, Republic of Gabon. Proc. XXVth Intern. Congr. Geology, Sydney (1976). In: Varensov, I.M., Gaassell, G.Y. (Eds.), Geology and Geochemitry of Manganese, 2. Schweitzerbart'sche Verl, Stutt-gart, Germany, pp. 89–109.

Little, S.H., Vance, D., Lyons, T.W., McManus, J., 2015. Controls on trace metal authigenic enrichment in reducing sediments: Insights from modern oxygen-deficient settings. Am. J. Sci. 315, 77–119.

Liu, W., Hao, J., Elzinga, E.J., Piotrowiak, P., Nanda, V., Yee, N., Falkowski, P.G., 2020. Anoxic photogeochemical oxidation of manganese carbonate yields manganese oxide. Proc. Natl. Acad. Sci. U. S. A. 117, 22698–22704.

Liu, X.M., Hardisty, D.S., Lyons, T.W., Swart, P.K., 2019. Evaluating the fidelity of the cerium paleoredox tracer during variable carbonate diagenesis on the Great Bahamas Bank. Geochim. Cosmochim. Acta 248, 25–42.

Liu, Y.G., Miah, M.R.U., Schmitt, R.A., 1988. Cerium: A chemical tracer for paleo-oceanic redox conditions. Geochim. Cosmochim. Acta 52, 1361–1371.

961 Lyons, T.W., Diamond, C.W., Konhauser, K.O., 2020. Shedding light on manganese cycling
962 in the early oceans. Proc. Natl. Acad. Sci. U. S. A. 117, 25960–25962.

963 Lyons, T.W., Reinhard, C.T., Planavsky, N.J., (2014). The rise of oxygen in Earth's early ocean
964 and atmosphere. Nature 506, 307–315.

965 Ma, Z., Liu, X., Yu, W., Du, Y., Du, Q., 2019. Redox conditions and manganese metallogenesis
966 in the Cryogenian Nanhua Basin: Insight from the basal Datangpo Formation of South China.
967 Palaeogeogr. Palaeoclimatol. Palaeoecol. 529, 39–52.

968 Mancini, F., Alviola, R., Marshall, B., Satoh, H., Papunen, H., 2000. The manganese silicate
969 rocks of the early Proterozoic Vittinki Group, southwestern Finland: Metamorphic grade and
970 genetic interpretations. Can. Mineral. 38, 1103–1124.

971 McLennan, S.M., Bock, B., Hemming, S.R., Hurowitz, J.A., Steven, M.L., and McDaniel,
972 D.K., 2003, The roles of provenance and sedimentary processes in the geochemistry of
973 sedimentary rocks, in Lentz, D.R., Ed., Geochemistry of sediments and sedimentary
974 rocks/evolutionary considerations to mineral deposit-forming environments: Geological
975 Association of Canada, p. 184.

976 Mänd, K., Robbins, L.J., Lalonde, S.V., Thoby, M., Paiste, K., Kreitsmann, T., Paiste,
977 P.,Reinhard, C.T., Romashkin, A.E., Kirsimäe, K., Lepland, A., Konhauser, K.O., 2020.
978 Paleoproterozoic oxygenated oceans following the Lomagundi-Jatuli Event. nat.Geosci. 13,
979 302–306.

980 Martins, G., Oliveira, E.P., Lafon, J.M., 2009. The Algod.es amphibolite–tonalite gneiss
981 sequence, Borborema Province, NE Brazil: geochemical and geochronological evidence for
982 Palaeoproterozoic accretion of oceanic plateau/back-arc basalts and adakitic plutons.
983 Gondwana Res. 15, 71–85.

984 Mayika, K.B., Moussavou, M., Prave, A.R., Lepland, A., Mbina, M., Kirsimäe, K., 2020. The
985 Paleoproterozoic Francevillian succession of Gabon and the Lomagundi-Jatuli event. Geology
986 48, 1099–1104.

987 Maynard, J.B., 2010. The chemistry of manganese ores through time: A signal of increasing
988 diversity of earth-surface environments. Econ. Geol. 105, 535–552.

989 McLennan S. M., 2001. Relationships between the trace element composition of sedimentary
990 rocks and upper continental crust. Geochem. Geophys. Geosys. 2 (article no. 2000GC000109).

991 McLennan, S. M., Taylor S. R., and Hemming S. R., 2001. Composition, differentiation, and
992 evolution of continen- tal crust: Constraints from sedimentary rocks and heat flow, in Evolution
993 and Differentiation of the Continental Crust, edited by M. Brown and T. Rushmer, Cambridge
994 Univ. Press, New York, in press.

995 Melezhik, V. A., Huhma, H., Condon, D. J., Fallick, A. E., & Whitehouse, M. J. (2007).
996 Temporal constraints on the Paleoproterozoic Lomagundi-Jatuli carbon isotopic
997 event. Geology, *35*(7), 655-658.

998 Menzies, M., Blanchard, D., & Jacobs, J. (1977). Rare earth and trace element geochemistry
999 of metabasalts from the Point Sal ophiolite, California. Earth and Planetary Science
1000 Letters, *37*(2), 203-215.

1001 Morford, J.L., Emerson, S., 1999. The geochemistry of redox sensitive trace metals in
1002 sediments. Geochim. Cosmochim. Acta 63, 1735–1750.

1003 Morse, J.W., Luther, G.W., 1999. Chemical influences on trace metal-sulfide interactions in
1004 anoxic sediments. Geochim. Cosmochim. Acta 63, 3373–3378.

1005 Mücke, A., Dzigbodi-Adjimah, K., Annor, A., 1999. Mineralogy, petrography, geochemistry
1006 and genesis of the Paleoproterozoic Birimian manganese-formation of Nsuta/Ghana. Miner.
1007 Depos. 34, 297–311.

1008 Navarro, M. S., Tonetto, E. M., & Oliveira, E. P. 2017. Peixe zircon: new Brazilian reference
1009 material for U-Pb geochronology by LA-SF-ICP-MS. In Goldschmidt Conference,.
1010 https://goldschmidtabstracts. info/2017/3815. pdf.

1011 Nesbitt, H.W., 2003, Petrogenesis of siliciclastic sediments and sedimentary rocks, in
1012 Lentz, D.R., Ed., Geochemistry of sediments and sedimentary rocks/evolutionary
1013 considerations to mineral deposit-forming environments, Volume 4: Geological Association of
1014 Canada GeoText, p. 39–51.

1015 Neves, S.P., 2003. Proterozoic history of the Borborema province (NE Brazil): Correlations
1016 with neighboring cratons and Pan-African belts and implications for the evolution of western
1017 Gondwana. Tectonics 22.

1018 Neves, S.P., 2011. Atlantica revisited: New data and thoughts on the formation and evolution
1019 of a long-lived continent. Int. Geol. Rev. 53, 1377–1391.

1020 Neves, S.P., Mariano, G., 1999. Assessing the tectonic significance of a large-scale transcurrent
1021 shear zone system: The Pernambuco lineament, northeastern Brazil. J. Struct. Geol. 21, 1369–
1022 1383.

1023 Nyame, F., 2001. Petrological significance of manganese carbonate inclusions in spessartine
1024 garnet and relation to the stability of spessartine in metamorphosed manganese-rich rocks.
1025 Contrib. To Mineral. Petrol. 141, 733–746.

1026 Ohta, A., Ishii, S., Sakakibara, M., Mizuno, A., Kawabe, I., 1999. Systematic correlation of the
1027 Ce anomaly with the Co/(Ni+Cu) ratio and Y fractionation from Ho in distinct types of Pacific
1028 deep-sea nodules. Geochem. J. 33, 399–417.

1029 Okita, P. M., Maynard, J. B., Spiker, E. C. and Force, E. R., 1988. Isotopic evidence for organic
1030 matter oxidation by manganese reduction in the formation of stratiform manganese carbonate
1031 ore. Geochim. Cosmochim. Acta, 52, 2679-2685.

1032 Orth C. J., Attrep, Jr., M., Quintana L. R., Elder W. P., Kauffman E. G., Diner R. and Villamil
1033 T. (1993) Elemental abundance anomalies in the late Cenomanian extinction interval: a search
1034 for the source(s). Earth Planet. Sci. Lett. 117, 189–204.

1035 Ossa Ossa, F., Eickmann, B., Hofmann, A., Planavsky, N.J., Asael, D., Pambo, F., Bekker, A.,
1036 2018. Two-step deoxygenation at the end of the Paleoproterozoic Lomagundi Event. Earth
1037 Planet. Sci. Lett. 486, 70–83.

1038 Paiste, K., Lepland, A., Zerkle, A.L., Kirsimäe, K., Izon, G., Patel, N.K., McLean, F.,
1039 Kreitsmann, T., Mänd, K., Bui, T.H., Romashkin, A.E., Rychanchik, D. V., Prave, A.R., 2018.
1040 Multiple sulphur isotope records tracking basinal and global processes in the 1.98 Ga Zaonega
1041 Formation, NW Russia. Chem. Geol. 499, 151–164.

Partin, C.A., Lalonde, S.V., Planavsky, N.J., Bekker, A., Rouxel, O.J., Lyons, T.W., Konhauser, K.O., 2013a. Uranium in iron formations and the rise of atmospheric oxygen. Chem Geol 362, 82 90.

Partin, C.A., Bekker, A., Planavsky, N.J., Scott, C.T., Gill, B.C., Li, C., Podkovyrov, V., Maslov, A., Konhauser, K.O., Lalonde, S.V., Love, G.D., Poulton, S.W., Lyons, T.W., 2013b. Large-scale fluctuations in Precambrian atmospheric and oceanic oxygen levels from the record of U in shales. Earth Planet Sc Lett 369-370, 284 293.

Paton, C., Hellstrom, J., Paul, B., Woodhead, J., and Hergt, J., 2011, Iolite: Freeware for the visualisation and processing of mass spectrometric data: Journal of Analytical Atomic Spectrometry, v. 26, p. 2508–2518.

Paton, C., Woodhead, J.D., Hellstrom, J.C., Hergt, J.M., Greig, A., and Maas, R., 2010, Improved laser ablation U-Pb zircon geochronology through robust downhole fractionation correction: Geochemistry Geophysics Geosystems, v. 11, p. Q0AA06.

Petrus, J.A., Kamber, B.S., 2012, VizualAge: A novel approach to Laser Ablation ICP-MS U-Pb Geochronology data reduction: Geostandards and Geoanalytical Research, v. 36, p. 247–270.

Pitarello, M.Z., Santos, T.J.S. do., Ancelmi, M.F., 2019. Syn-to post-depositional processes related to high grade metamorphic BIFs: Geochemical and geochronological evidences from a Paleo to Neoarchean (3.5–2.6 Ga) terrane in NE Brazil. J. South Am. Earth Sci. 96, 102312.

Planavsky, N.J., Bekker, A., Rouxel, O.J., Kamber, B., Hofmann, A., Knudsen, A., Lyons, T. W., 2010. Rare earth element and yttrium compositions of Archean and Paleoproterozoic Fe formations revisited: New perspectives on the significance and mechanisms of deposition: Geochim. Cosmochim. Acta, 74, 6387–6405.

Planavsky, N.J., Slack, J.F., Cannon, W.F., O'Connell, B., Terry-Tang, Y., Asael, D.,Jackson, J.C., Hardisty, D.S., Lyons, T.W., Bekker, A., 2018. Evidence for episodic oxygenation in a weakly redox-buffered deep mid-Proterozoic ocean. Chem. Geol.

Polgári, M., Hein, J.R., Toth, A.L., Pal-Molnár, E., Vigh, T., Biró, L., Fintor, K., 2012. Microbial action formed Jurassic Mn-carbonate ore deposit in only a few hundred years (Úrkút, Hungary). Geology 40, 903–906.

Post, J.E., 1999. Manganese oxide minerals: crystal structures and economic and environmental significance. Proc. Natl. Acad. Sci. 96, 3447–3454.

Poulton, S. W., Bekker, A., Cumming, V. M., Zerkle, A. L., Canfield, D. E., Johnston, D. T. (2021). A 200-million-year delay in permanent atmospheric oxygenation. Nature, 592(7853), 232-236.

Robbins, L.J., Lalonde, S.V., Planavsky, N.J., Partin, C.A., Reinhard, C.T., Kendall, B., Scott, C., Hardisty, D.S., Gill, B.C., Alessi, D.S. and Dupont, C.L., (2016). Trace elements at the intersection of marine biological and geochemical evolution. Earth-Science Reviews.

Rosa-Costa, L.T., Lafon, J.M., Delor, C., 2006. Zircon geochronology and Sm-Nd isotopic study: Further constraints for the Archean and Paleoproterozoic geodynamical evolution of the southeastern Guiana Shield, north of Amazonian Craton, Brazil. Gondwana Res. 10, 277–300.

Roy, S., 2006. Sedimentary manganese metallogenesis in response to the evolution of the Earth system. Earth-Science Rev. 77, 273–305.

Rudnick, R. L. (1992). Restites, Eu anomalies and the lower continental crust. Geochimica et Cosmochimica Acta, 56(3), 963-970.

Santos, F.H., Amaral, W.S., Konhauser, K., Martins, D.T., Castro, M.P., Queiroga, G.N., Chi-Fru, E., Andersen, M.B., 2021. Unraveling sedimentary precursors and metal enrichment of high-grade metamorphosed manganese-rich rocks from the Borborema Province, northeastern Brazil. Ore Geol Rev 137:104283.

Scott, C., Lyons, T.W., Bekker, A., Shen, Y., Poulton, S.W., Chu, X., Anbar, A.D., 2008. Tracing the stepwise oxygenation of the Proterozoic ocean. Nature 452, 456 459.

Shields, G., Stille, P., 2001. Diagenetic constraints on the use of cerium anomalies as palaeoseawater redox proxies: an isotopic and REE study of Cambrian phosphorites. Chem. Geol. Response of the Oceanic/Atmospheric Systems to Past Global Changes 175, 29–48.

Schier, K et al., 2020. Chemical evolution of seawater in the Transvaal Ocean between 2426Ma (Ongeluk Large Igneous Province) and 2413 Ma ago (Kalahari Manganese Field). Gondwana Research, 88, 373-388.

Slack, J.F., Shaw, D.R., Leitch, C.H.B., and Turner, R.J.W., 2000, Tourmalinites and coticules from the Sullivan Pb-Zn-Ag deposit and vicinity, British Columbia: Geology, geochemistry, and genesis, in Lydon, J.W., et al., eds., Geological environment of the Sullivan deposit, British Columbia: Geological Association of Canada Mineral Deposits Division Special Publication 1, 736–767.

Smith, A.J.B., Beukes, N.J., Gutzmer, J., 2013. The Composition and Depositional Environments of Mesoarchean Iron Formations of the West Rand Group of the Witwatersrand Supergroup, South Africa. Econ. Geol. v. 108, pp. 111–134.

Sousa, H.P., Parente, C.V., Magini, C., Ximenes, D.R.B., Dantas, E.L., Caby, R., Rosa Júnior, C.A., 2019. History of volcanism and sedimentation synchronous with plutonism during Rhyacian in Serra das Pipocas Greenstone Belt, Borborema Province, NE Brazil. J. South Am. Earth Sci. 95, 102220.

Souza, J.V. de; Ribeira Filho, E. 1983. Geologia e Gênese dos Depósitos de Manganês da Província de Aracoiaba - Pacajús, Ceará. Revista do Instituto de Geociências - Usp, São Paulo. 14, 1-11.

Souza, Z.S., Kalsbeek, F., Deng, X.D., Frei, R., Kokfelt, T.F., Dantas, E.L., Li, J.W., Pimentel, M.M., Galindo, A.C., 2016. Generation of continental crust in the northern part of the Borborema Province, northeastern Brazil, from Archaean to Neoproterozoic. J. South Am. Earth Sci. 68, 68–96.

Spencer, C.J., Kirkland, C.L., Taylor, R.J.M., 2016. Strategies towards statistically robust interpretations of in situ U-Pb zircon geochronology. Geoscience Frontiers 7 (37), pp. 581–589.

Spry, P.G., Peters, J. & Slack, J.F., 2000. Meta-exhalites as keys in the search for metamorphosed ore deposits. In Metamorphosed and Metamorphogenic Ore Deposits (P.G. Spry, B. Marshall & F.M. Vokes, eds.). Rev. Econ. Geol. 11, 163-201.

Steadman, J.A., Spry, P.G., 2015. Metamorphosed proterozoic Zn-Pb-Ag mineralization in the Foster River area, Northern Saskatchewan, Canada. Econ. Geol. 110, 1193–1214.

Takahashi, S., Yamasaki, S.-i., Ogawa, Y., Kimura, K., Kaiho, K., Yoshida, T., Tsuchiya, N., 2014. Bioessential element-depleted ocean following the euxinic maximum of the end-Permian mass extinction. Earth Planet. Sci. Lett. 393, 94–104.

Tashiro, T., Ishida, A., Hori, M., Igisu, M., Koike, M., Méjean, P., Takahata, N., Sano, Y., Komiya, T., 2017. Early trace of life from 3.95 Ga sedimentary rocks in Labrador, Canada. Nature 549, 516-518.

Taylor, S.R., McLennan, S.M., 1985. The continental crust: Its composition and evolution. Blackwell, Oxford.

Tebo B.M., Johnson H.A., McCarthy J.K., Templeton A.S., 2005. Geomicrobiology of manganese (II) oxidation. Trends Microbiol. 13, 421–428.

Teixeira, N.L., Caxito, F.A., Rosière, C.A., Pecoits, E., Vieira, L., Frei, R., Sial, A.N., Poitrasson, F., 2017a. Trace elements and isotope geochemistry (C, O, Fe, Cr) of the Cauê iron formation, Quadrilátero Ferrífero, Brazil: Evidence for widespread microbial dissimilatory iron reduction at the Archean/Paleoproterozoic transition. Precambrian Res. 298, 39–55.

Teixeira, W., Oliveira, E.P., Peng, P., Dantas, E.L., Hollanda, M.H.B.M., 2017b. U-Pb geochronology of the 2.0 Ga Itapecerica graphite-rich supracrustal succession in the São Francisco Craton: Tectonic matches with the North China Craton and paleogeographic inferences. Precambrian Res. 293, 91–111. https://doi.org/10.1016/j.precamres.2017.02.021

Torres, P.F.M., Cavalcante, J.C., Palheta, E.S.M., Vasconcelos, A.M., Oliveira, F.V., 2007. Folha Quixada. Folha SB-24-V-B, Escala 1:250.000. Geologia e Metalogênese. In: Programa Levantamentos Geologicos Basicos do Brasil. Fortaleza: Serviço Geologico do Brasil. CPRM.

Torsvik, T.H., Cocks, L.R.M., 2013. Gondwana from top to base in space and time. Gondwana Res. 24, 999–1030.

Tostevin, R., Shields, G.A., Tarbuck, G.M., He, T., Clarkson, M.O., Wood, R.A., 2016a. Effective use of cerium anomalies as a redox proxy in carbonate-dominated marine settings. Chem. Geol. 438, 146–162.

Tostevin, R., Wood, R.A., Shields, G.A., Poulton, S.W., Guilbaud, R., Bowyer, F., Penny, A.M., He, T., Curtis, A., Hoffmann, K.H., Clarkson, M.O., 2016b. Low-oxygen waters limited habitable space for early animals. Nat. Commun. 7.

Tribovillard, N., 2020. Arsenic in marine sediments: how robust a redox proxy? Palaeogeogr. Palaeoclimatol. Palaeoecol. 550, 109745.

Tribovillard, N., Algeo, T.J., Lyons, T., Riboulleau, A., 2006. Trace metals as paleoredox and paleoproductivity proxies: An update. Chem. Geol. 232, 12–32.

Towell, D. G., Spirn, R. V., & Winchester, J. W. (1969). Europium anomalies and the genesis of basalt: a discussion. Chemical Geology, *4*(3-4), 461-464.

van Helmond, N.A.G.M., Jilbert, T., Slomp, C.P., 2018. Hypoxia in the Holocene Baltic Sea: Comparing modern versus past intervals using sedimentary trace metals. Chem. Geol. 493, 478–490.

Vasquez, M.L., Macambira, M.J.B., Armstrong, R.A., 2008. Zircon geochronology of granitoids from the western Bacajá domain, southeastern Amazonian craton, Brazil: Neoarchean to Orosirian evolution. Precambrian Res. 161, 279–302.

Vauchez, A., Neves, S., Caby, R., Corsini, M., Egydio-Silva, M., Arthaud, M., Amaro, V., 1995. The Borborema shear zone system, NE Brazil. J. South Am. Earth Sci. 8, 247–266.

Vermeesch, P., 2018, IsoplotR: a free and open toolbox for geochronology. Geoscience Frontiers, 9, 1479-1493.

Viegas, L.G.F., Archanjo, C.J., Hollanda, M.H.B.M., Vauchez, A., 2014. Microfabrics and zircon U-Pb (SHRIMP) chronology of mylonites from the Patos shear zone (Borborema Province, NE Brazil). Precambrian Res. 243, 1–17.

Warke, M.R., Strauss, H., Schröder, S., 2020. Positive cerium anomalies imply pre-GOE redox stratification and manganese oxidation in Paleoproterozoic shallow marine environments. Precambrian Res. 344, 105767.

Warke, M.R., Rocco, T.D., Zerkle, A.L., Lepland, A., Prave, A.R., Martin, A.P., Ueno, Y., Condon, D.J., Claire, M.W., 2020. The Great Oxidation Event preceded a Paleoproterozoic "snowball Earth." Proc National Acad Sci 117, 13314-13320.

Wei, G., Liu, Y., Li, X., Shao, L., Liang, X., 2003. Climatic impact on Al, K, Sc and Ti in marine sediments: Evidence from ODP site 1144, South China Sea. Geochem J 37:593–602.

Wiedenbeck M., Allé P., Corfu F., Griffin W., Meier M., Oberli F., von Quadt A., Roddick J.C. and Spiegel W.,1995. Three natural zircon standards for U-Th-Pb, Lu-Hf, trace element and REE analyses. Geostandards Newsletter, 19, 1–23

Wu, C., Zhang, Z., Xiao, J., Fu, Y., Shao, S., Zheng, C., Yao, J., Xiao, C., 2016. Nanhuan manganese deposits within restricted basins of the southeastern Yangtze Platform, China: constraints from geological and geochemical evidence. Ore Geol. Rev. 75, 76–99.

Xiao, J.F., He, J.Y., Yang, H.Y., Wu, C., 2017. Comparison between Datangpo-type manganese ores and modern marine ferromanganese oxyhydroxide precipitates based on rare earth elements. Ore Geol. Rev. 89, 290–308.

Zerkle, A. L., Poulton, S. W., Newton, R. J., 2 , Mettam, C., Claire, M. W., Bekker, A., Junium, C. K. 2017. Onset of the aerobic nitrogen cycle during the Great Oxidation Event. Nature 542, 465–467.

Zhang, B.-L., Wang, C.-L., Robbins, L.J., Zhang, L.-C., Konhauser, K.O., Dong, Z.-G., Li, W.-J., Peng, Z.-D., Zheng, M.-T., 2020. Petrography and Geochemistry of the Carboniferous Ortokarnash Manganese Deposit in the Western Kunlun Mountains, Xinjiang Province, China: Implications for the Depositional Environment and the Origin of Mineralization. Econ. Geol. 115, 1559–1588.

Zhang, B., Yao, S., Hu, W., Ding, H., Liu, B., Ren, Y., 2019. Development of a high-productivity and anoxic-euxinic condition during the late Guadalupian in the Lower Yangtze region: Implications for the mid-Capitanian extinction event. Palaeogeogr. Palaeoclimatol. Palaeoecol. 531, 108630.

Figure captions

Fig. 1. Simplified map of the Borborema Province (Northeast Brazil) within the West Gondwana and location of study area. (A) West Gondwana in the Middle Paleozoic with the Borborema Province location within the black line: 1 = Amazonian Craton; 2= São Francisco Craton; 3= São Luís Craton; 4= West African Craton; and 5= Congo Craton. Modified from Cordani et al. (2016). (B) Geological framework of the Northern Borborema Province (according to Brito Neves et al., 2000) highlighting study area in white star. MCD= Médio Coreaú Domain; CCD= Ceará Central Domain; TBL= Transbrasiliano Lineament; OASZ= Orós-Aiuaba Shear Zone; PSZ= Patos Shear Zone. (C) Local map of the Lagoa do Riacho manganese deposit (left) and schematic cross-section constructed from the core Ocr-1 (right) showing location of sample collected for U-Pb geochronology and the distribution of the manganese-rich lithological groups investigated in the present study. Core Ocr-1 is from the Open pit 3.

Fig. 2. A-D from MSR group; E-G from manganese-quartzite; H and I from garnetite. Hand-specimen photographs of the SMR and manganese-quartzite (A and E), respectively. Transmitted (B and I; under cross polarized) and reflected (G) light photomicrographs for the SMR, manganese-quartzite and garnetite. BSE (C, D, F and H) images showing petrographic aspects for all lithological groups. (A) Matrix minerals composed mainly (>70%) of coarse-grained manganese-pyroxene (Pxmn). (B) Manganese-pyroxene porphyroblast in contact with garnet-spessartine (Spss) and carbonate (Carb), defining a granoblastic texture. (C) Minor spots of manganese-oxide-hydroxide minerals (Mn-oh) replacing manganese-pyroxene. Spessartine garnet in contact with manganese-pyroxene. Diminute pyrite (Pyr) in contact with graphite (Gph) flakes. (D) Cobaltite (Cb; CoAsS) in triple contact with manganese-pyroxene and spessartine. (E) Graphite flakes distributed through fine-grained rock matrix composed of quartz-feldspar (Qtz-Fsp). (F) Graphite along foliation planes in contact with pyrite, spessartine and quartz-feldspar agglomerates. (G) Stretched pyrite in close relationship with graphite flakes. (H) Spessartine garnet porphyroblast, interstitial quartz-feldspar and mica. (I) Carbonate, spessartine and manganese-pyroxene in a granoblastic texture.

Fig. 3. Boxplot with the enrichment factors of selected trace metals investigated here. The filled gray line through EF=1 represents normal values concerning the crustal average (e.g., PAAS).

Fig. 4. Correlation matrix plots of major oxide elements for the manganese-bearing groups investigated in this work. Crustal average (e.g., PAAS) was plotted for comparison.

Fig. 5. Correlation matrix plots of trace elements for the manganese-bearing rocks. Crustal averages (e.g., PAAS and UCC) were plotted for comparison.

Fig. 6. Rare-earth elements (REE) patterns. In (a) and (b) rare-earth element concentrations normalized to the PAAS (Taylor and McLennan, 1985; McLennan et al., 2001; McLennan, 2001).

Fig. 7. Binary-plot of $(Ce/Ce^*)_{SN}$ vs $(Pr/Pr^*)_{SN}$ for the manganese-bearing rock samples from this study. Data are normalized to average Post-Archean Australian Shale (PAAS; Taylor and McLennan, 1985; McLennan et al., 2001; McLennan, 2001). Fields after Bau and Dulski (1996). Samples of manganese-bearing stromatolite from Planavsky et al. (2010) are plotted for comparison.

Fig. 8. Geochronological data for the graphite-bearing pelitic gneiss (#10029). (A) Selected cathodoluminescence images for representative metamorphic zircons. Red circles represent the laser spot location (25 μm) of the U-Pb analysis. (B) General concordia diagram for the U-Pb zircon analyses. (C) General histogram with age and relative probability for the zircon grains selected for this study. (D) Concordia diagram for the metamorphic zircons. (E) Concordia diagram for the youngest concordant population.

Fig. 9. Proxies for linking the manganese-rich rocks to source area. (a) A-CN-K ternary diagram vs. chemical index of alteration (CIA) for the manganese-bearing rocks (Fedo et al. 1995; Nesbitt, 2003). The green circle represents a MORB average composition from Albarède (2005). $A = Al_2O_3$, $CN = CaO^* + Na_2O$, $K = K_2O$, Ka = kaolinite, Gib = gibbsite, Sm = smectite, Ms = muscovite, Pl = plagioclase, Kfs = K-feldspar, Hbl - hornblende. (b) Relationship between Th/Sc and Zr/Sc and the UCC contribution of Mn deposition (McLennan et al. 2003). The samples preferentially show a magmatic compositional variation trend.

Fig. 10. Cross-plots of the U and Mo enrichment factors (EF), according to Algeo and Tribovillard (2009). Note the arrow indicating a particulate shuttle from suboxic to euxinic waters. This process occurs in weakly restricted basin, such as the Cariaco Basin and Holocene

1270 Baltic Sea.
1271
1272 **Fig. 11.** A redox deposition model for the manganese-bearing rocks from the Northern
1273 Borborema Province. The model involves an upwelling of Mn reduced particles across a
1274 chemocline toward to oxic surface waters as well a Mn-oxide shuttle mechanism. At this
1275 model, manganese and cerium are oxidized on the oxic zone (Ce/Ce*<1) and subsequently
1276 reduced and incorporated in the bottom sediments at the anoxic/euxinic zone (Ce/Ce*<1).
1277 Manganese reduction takes place through the chemocline. Likely sedimentary precursors of
1278 the manganese rocks are also showed in the model. The behaviors of other trace metals present
1279 in this model (e.g., molybdenum and arsenic) are discussed in the next section. An inferred
1280 primary source for the metals, through submarine weathering of a basaltic rock, is also showed
1281 in the figure.
1282
1283

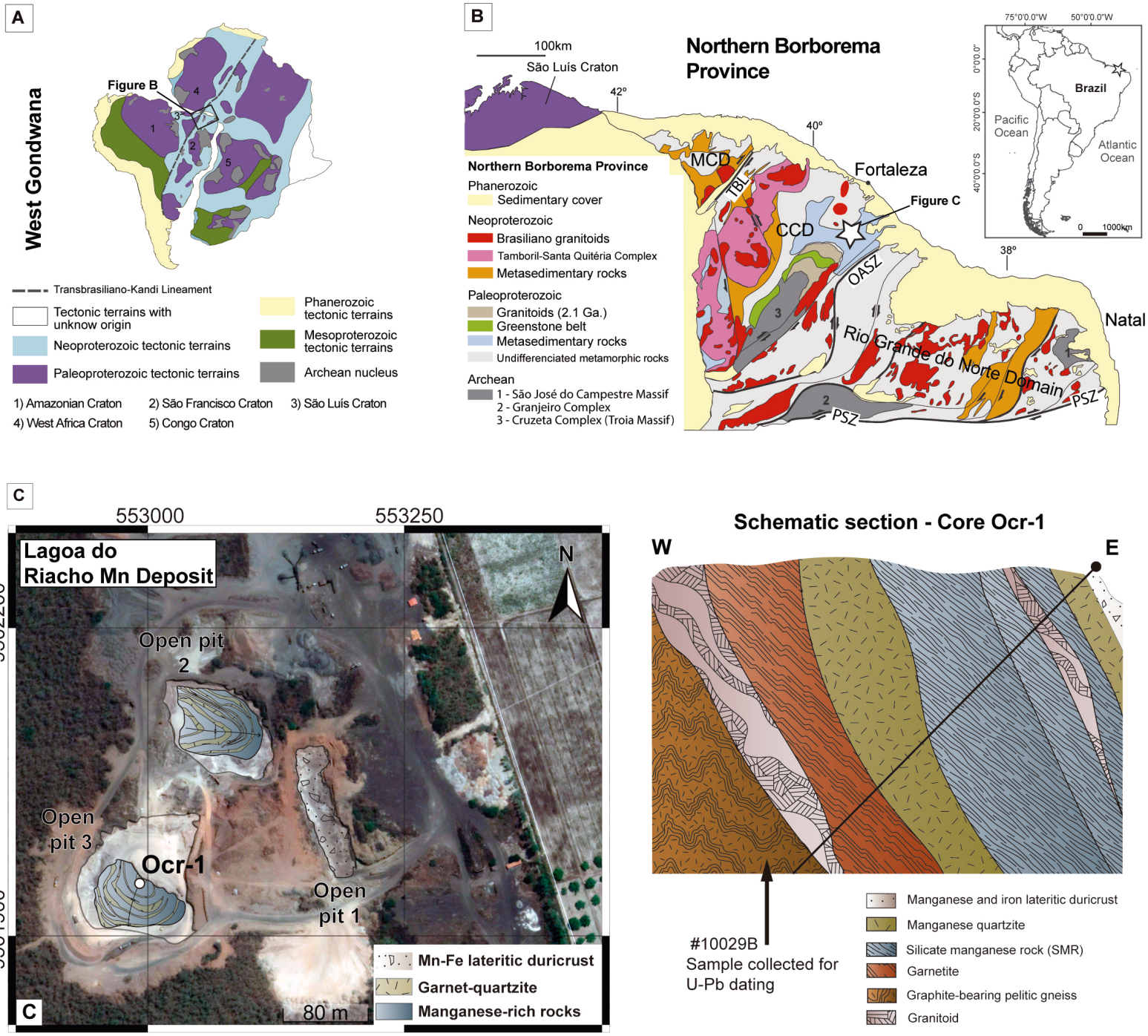
A
West Gondwana
Figure B
1
2
3
4
5
Transbrasiliano-Kandi Lineament
Tectonic terrains with unknow origin
Neoproterozoic tectonic terrains
Paleoproterozoic tectonic terrains
Phanerozoic tectonic terrains
Mesoproterozoic tectonic terrains
Archean nucleus
1) Amazonian Craton
2) São Francisco Craton
3) São Luís Craton
4) West Africa Craton
5) Congo Craton
B
100km
São Luís Craton
42°
40°
38°
Northern Borborema Province
MCD
TBL
CCD
OASZ
Fortaleza
Figure C
Natal
Rio Grande do Norte Domain
PSZ
PSZ
Northern Borborema Province
Phanerozoic
Sedimentary cover
Neoproterozoic
Brasiliano granitoids
Tamboril-Santa Quitéria Complex
Metasedimentary rocks
Paleoproterozoic
Granitoids (2.1 Ga.)
Greenstone belt
Metasedimentary rocks
Undifferenciated metamorphic rocks
Archean
1 - São José do Campestre Massif
2 - Granjeiro Complex
3 - Cruzeta Complex (Troia Massif)
75°0'0.0"W
50°0'0.0"W
0°0'0.0"
20°0'0.0"S
40°0'0.0"S
Brazil
Pacific Ocean
Atlantic Ocean
0
1000km
C
553000
553250
9502200
9501900
Lagoa do Riacho Mn Deposit
N
Open pit 2
Open pit 3
Ocr-1
Open pit 1
80 m
Mn-Fe lateritic duricrust
Garnet-quartzite
Manganese-rich rocks
Schematic section - Core Ocr-1
W
E
#10029B
Sample collected for U-Pb dating
Manganese and iron lateritic duricrust
Manganese quartzite
Silicate manganese rock (SMR)
Garnetite
Graphite-bearing pelitic gneiss
Granitoid

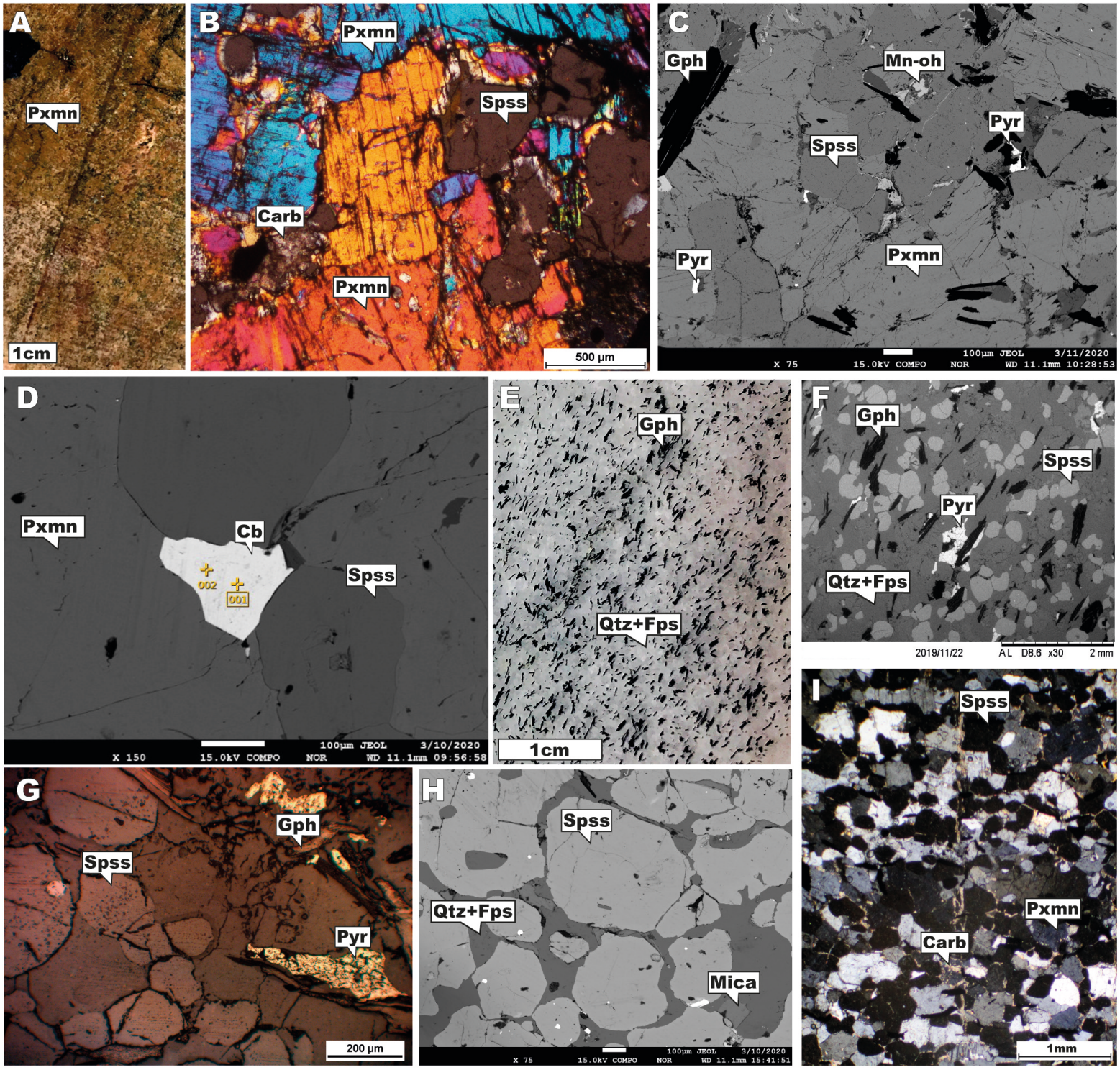
A
Pxmn
1cm
B
Pxmn
Spss
Carb
Pxmn
500 µm
C
Gph
Mn-oh
Pyr
Spss
Pyr
Pxmn
100µm JEOL 3/11/2020
X 75 15.0kV COMPO NOR WD 11.1mm 10:28:53
D
Pxmn
Cb
002
001
Spss
X 150 100µm JEOL 3/10/2020
15.0kV COMPO NOR WD 11.1mm 09:56:58
E
Gph
Qtz+Fps
1cm
F
Gph
Spss
Pyr
Qtz+Fps
2019/11/22 AL D8.6 x30 2 mm
G
Gph
Spss
Pyr
200 µm
H
Spss
Qtz+Fps
Mica
100µm JEOL 3/10/2020
X 75 15.0kV COMPO NOR WD 11.1mm 15:41:51
I
Spss
Pxmn
Carb
1mm

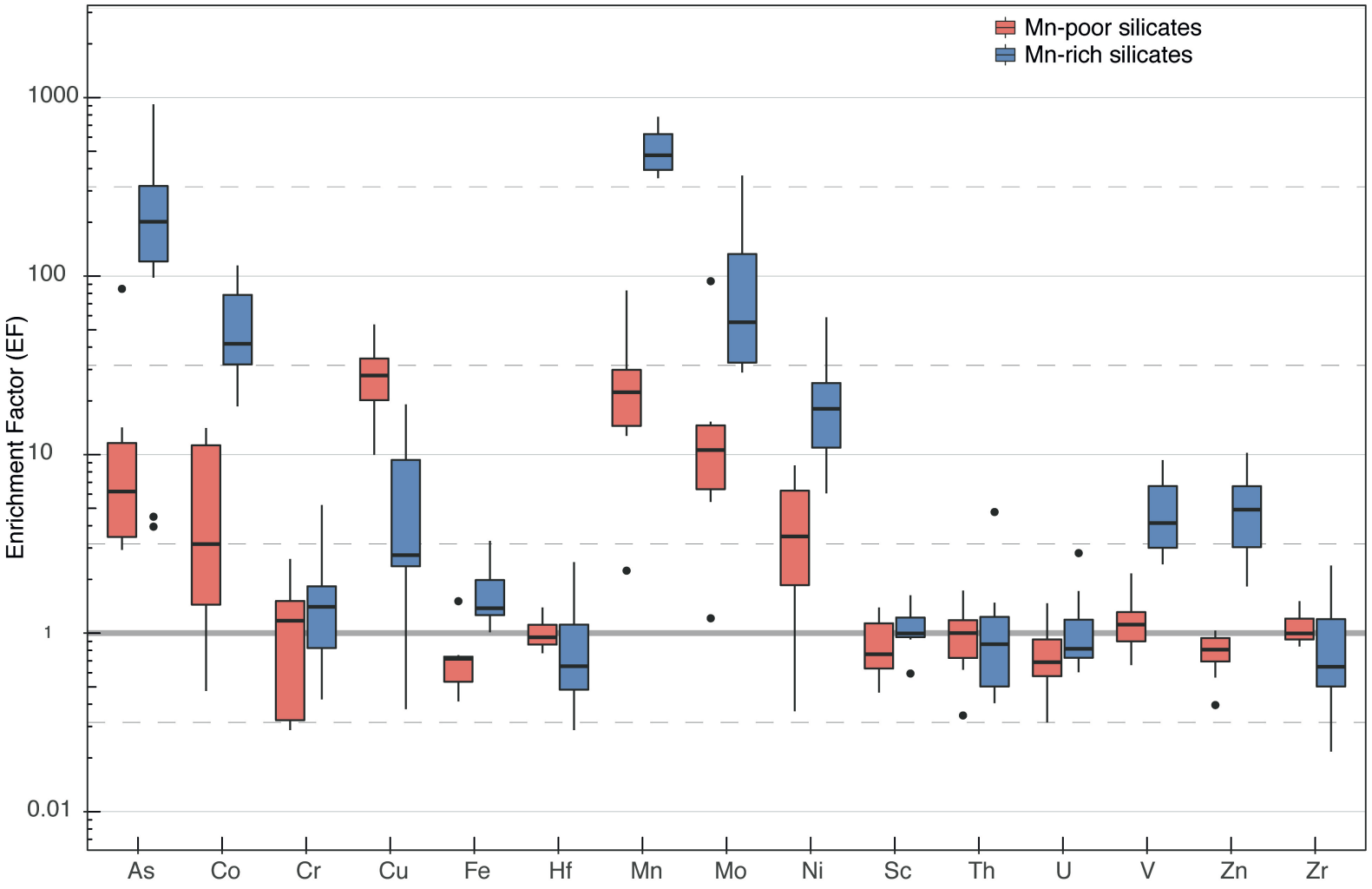
Mn-poor silicates
Mn-rich silicates
Enrichment Factor (EF)
1000
100
10
1
0.01
As
Co
Cr
Cu
Fe
Hf
Mn
Mo
Ni
Sc
Th
U
V
Zn
Zr

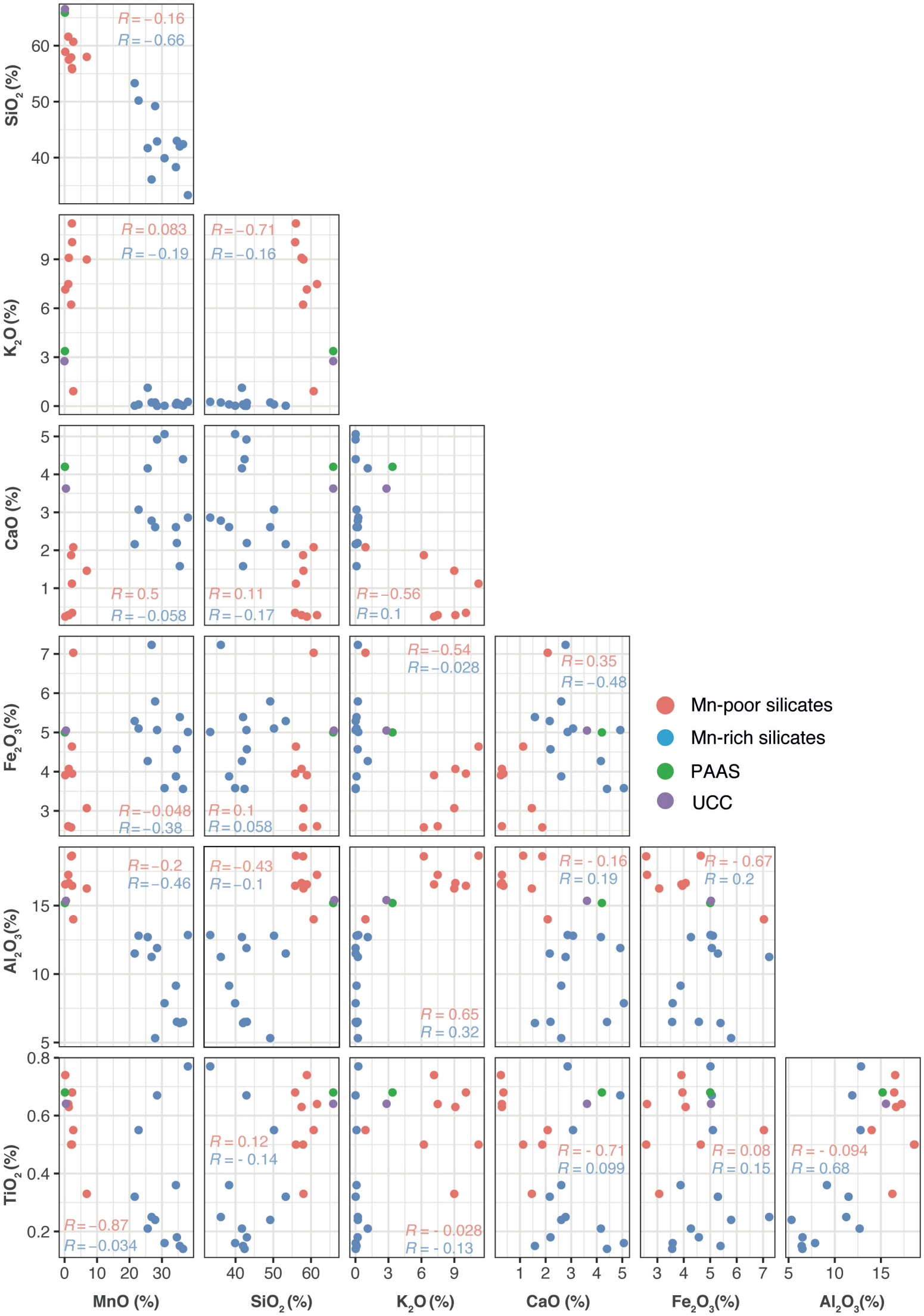
R = −0.16
R = −0.66
R = 0.083
R = −0.19
R = −0.71
R = −0.16
R = 0.5
R = −0.058
R = 0.11
R = −0.17
R = −0.56
R = 0.1
R = −0.54
R = −0.028
R = 0.35
R = −0.48
R = −0.048
R = −0.38
R = 0.1
R = 0.058
R = −0.2
R = −0.46
R = −0.43
R = −0.1
R = 0.65
R = 0.32
R = - 0.16
R = 0.19
R = - 0.67
R = 0.2
R = −0.87
R = −0.034
R = 0.12
R = - 0.14
R = - 0.028
R = - 0.13
R = - 0.71
R = 0.099
R = 0.08
R = 0.15
R = - 0.094
R = 0.68
Mn-poor silicates
Mn-rich silicates
PAAS
UCC
SiO2 (%)
K2O (%)
CaO (%)
Fe2O3(%)
Al2O3(%)
TiO2 (%)
MnO (%)
SiO2 (%)
K2O (%)
CaO (%)
Fe2O3(%)
Al2O3(%)

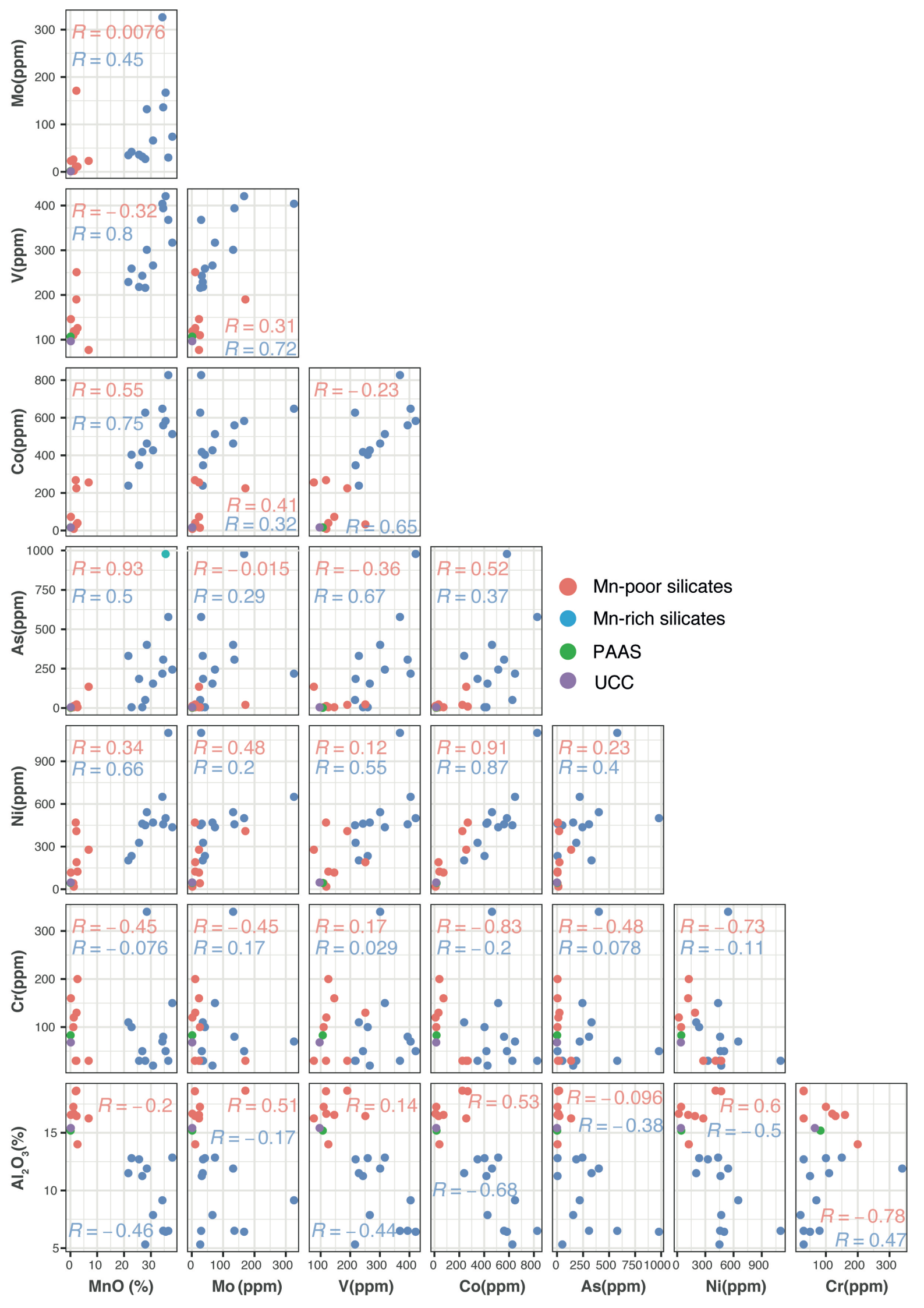
Mo(ppm)
V(ppm)
Co(ppm)
As(ppm)
Ni(ppm)
Cr(ppm)
Al2O3(%)
MnO (%)
Mo (ppm)
V(ppm)
Co(ppm)
As(ppm)
Ni(ppm)
Cr(ppm)
R = 0.0076
R = 0.45
R = −0.32
R = 0.8
R = 0.31
R = 0.72
R = 0.55
R = 0.75
R = −0.23
R = 0.41
R = 0.32
R = 0.65
R = 0.93
R = 0.5
R = −0.015
R = 0.29
R = −0.36
R = 0.67
R = 0.52
R = 0.37
R = 0.34
R = 0.66
R = 0.48
R = 0.2
R = 0.12
R = 0.55
R = 0.91
R = 0.87
R = 0.23
R = 0.4
R = −0.45
R = −0.076
R = −0.45
R = 0.17
R = 0.17
R = 0.029
R = −0.83
R = −0.2
R = −0.48
R = 0.078
R = −0.73
R = −0.11
R = −0.2
R = −0.46
R = 0.51
R = −0.17
R = 0.14
R = −0.44
R = 0.53
R = −0.68
R = −0.096
R = −0.38
R = 0.6
R = −0.5
R = −0.78
R = 0.47
Mn-poor silicates
Mn-rich silicates
PAAS
UCC

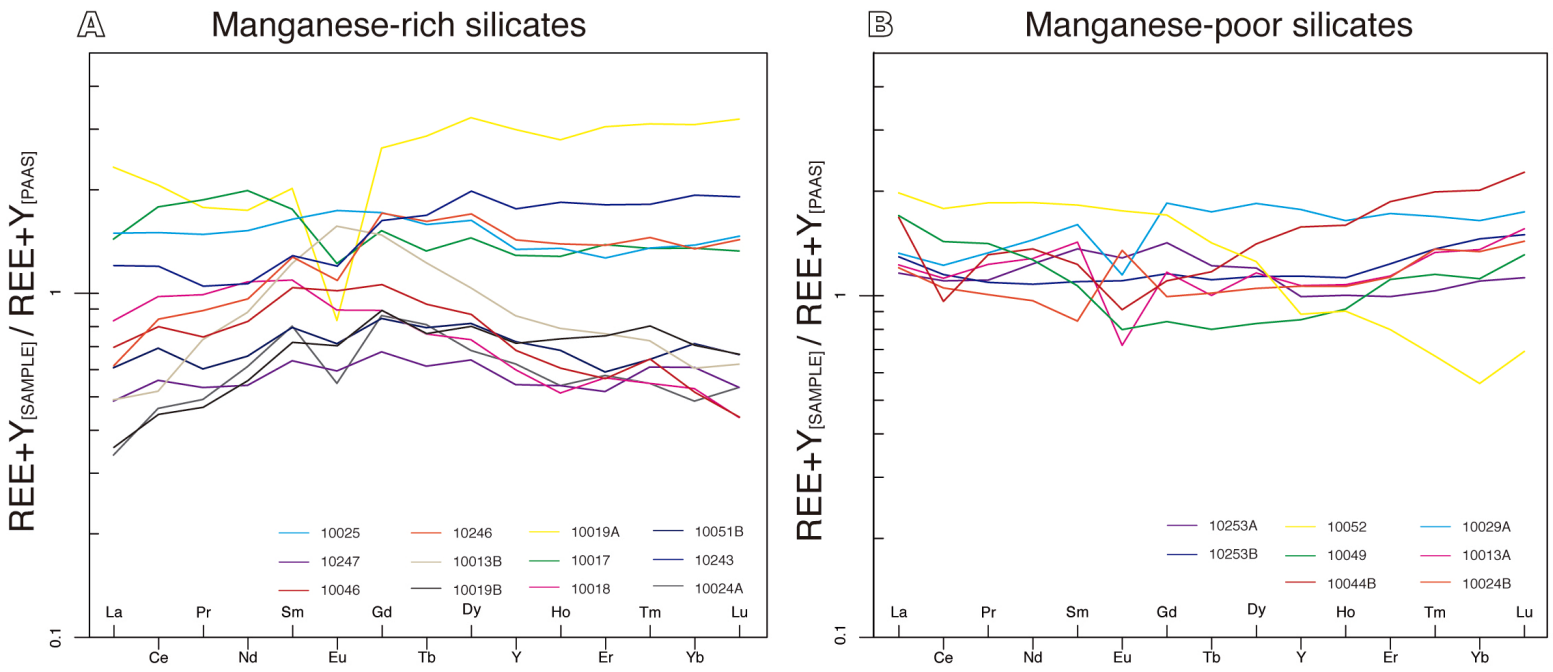
A
Manganese-rich silicates
REE+Y[SAMPLE] / REE+Y[PAAS]
1
0.1
10025
10246
10019A
10051B
10247
10013B
10017
10243
10046
10019B
10018
10024A
La
Pr
Sm
Gd
Dy
Ho
Tm
Lu
Ce
Nd
Eu
Tb
Y
Er
Yb
B
Manganese-poor silicates
REE+Y[SAMPLE] / REE+Y[PAAS]
1
0.1
10253A
10052
10029A
10253B
10049
10013A
10044B
10024B
La
Pr
Sm
Gd
Dy
Ho
Tm
Lu
Ce
Nd
Eu
Tb
Y
Er
Yb

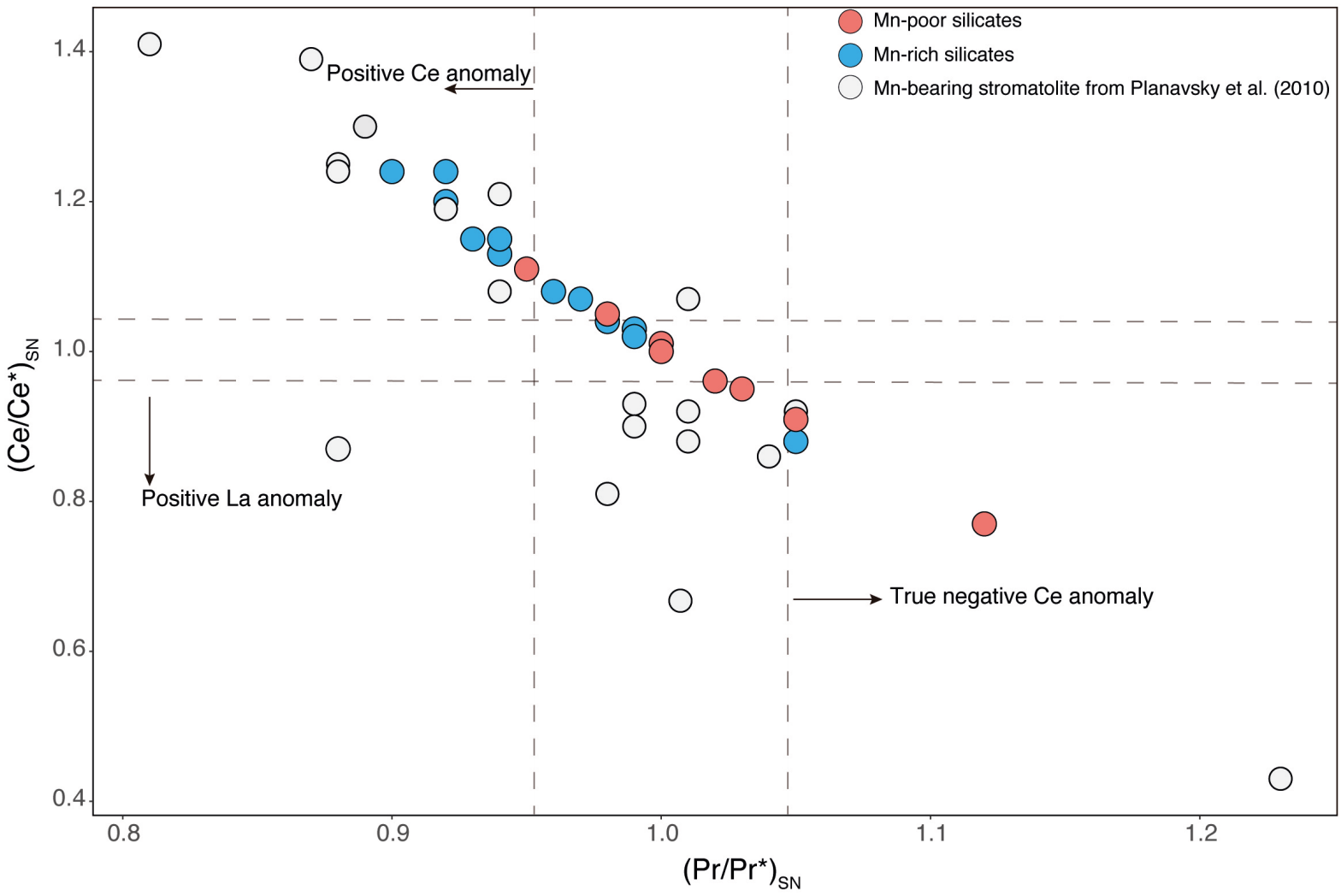
Mn-poor silicates
Mn-rich silicates
Mn-bearing stromatolite from Planavsky et al. (2010)
Positive Ce anomaly
Positive La anomaly
True negative Ce anomaly
(Ce/Ce*)SN
(Pr/Pr*)SN
1.4
1.2
1.0
0.8
0.6
0.4
0.8
0.9
1.0
1.1
1.2

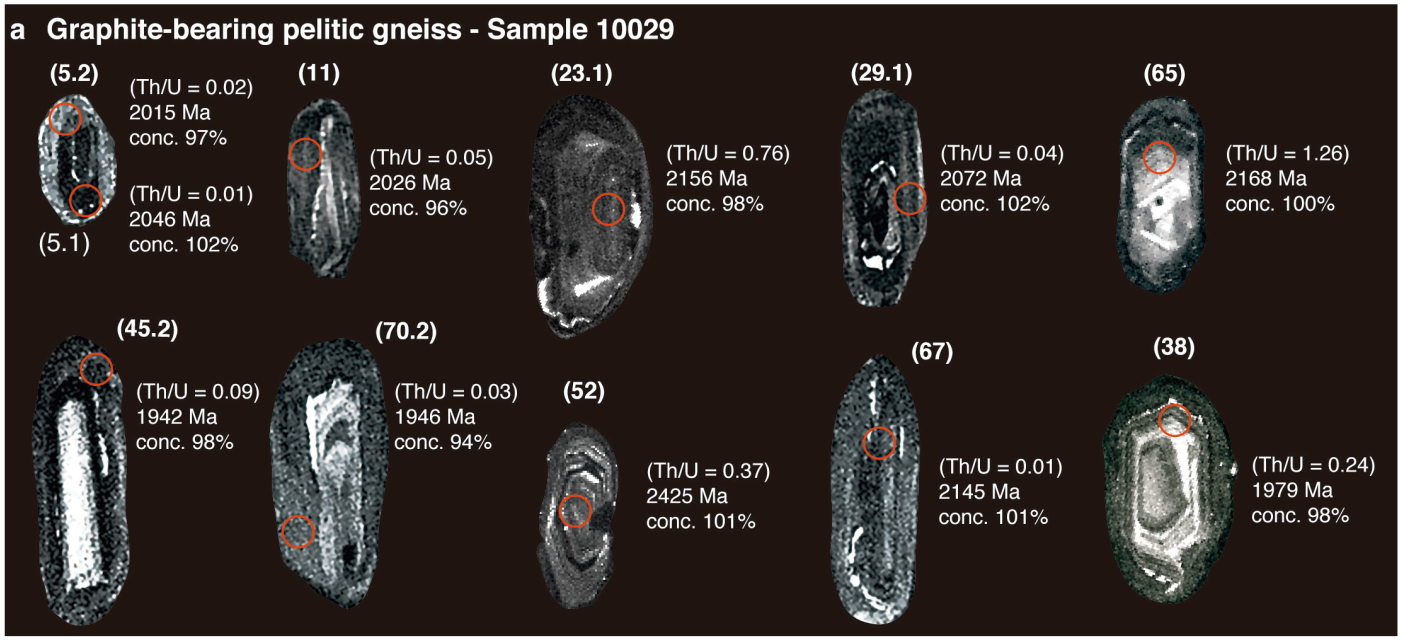
a Graphite-bearing pelitic gneiss - Sample 10029
(5.2)
(Th/U = 0.02)
2015 Ma
conc. 97%
(5.1)
(Th/U = 0.01)
2046 Ma
conc. 102%
(11)
(Th/U = 0.05)
2026 Ma
conc. 96%
(23.1)
(Th/U = 0.76)
2156 Ma
conc. 98%
(29.1)
(Th/U = 0.04)
2072 Ma
conc. 102%
(65)
(Th/U = 1.26)
2168 Ma
conc. 100%
(45.2)
(Th/U = 0.09)
1942 Ma
conc. 98%
(70.2)
(Th/U = 0.03)
1946 Ma
conc. 94%
(52)
(Th/U = 0.37)
2425 Ma
conc. 101%
(67)
(Th/U = 0.01)
2145 Ma
conc. 101%
(38)
(Th/U = 0.24)
1979 Ma
conc. 98%

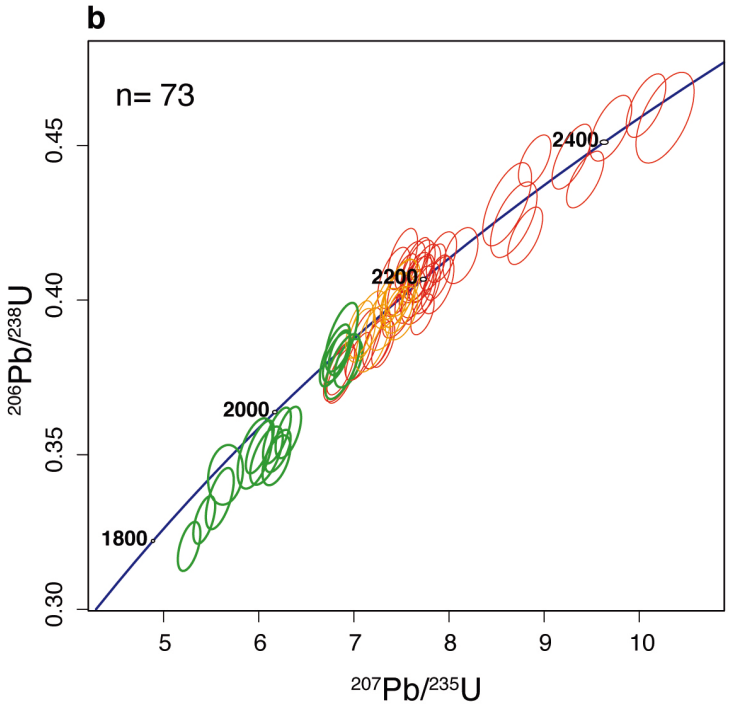
b
n= 73
2400
2200
2000
1800
0.30
0.35
0.40
0.45
5
6
7
8
9
10
206Pb/238U
207Pb/235U

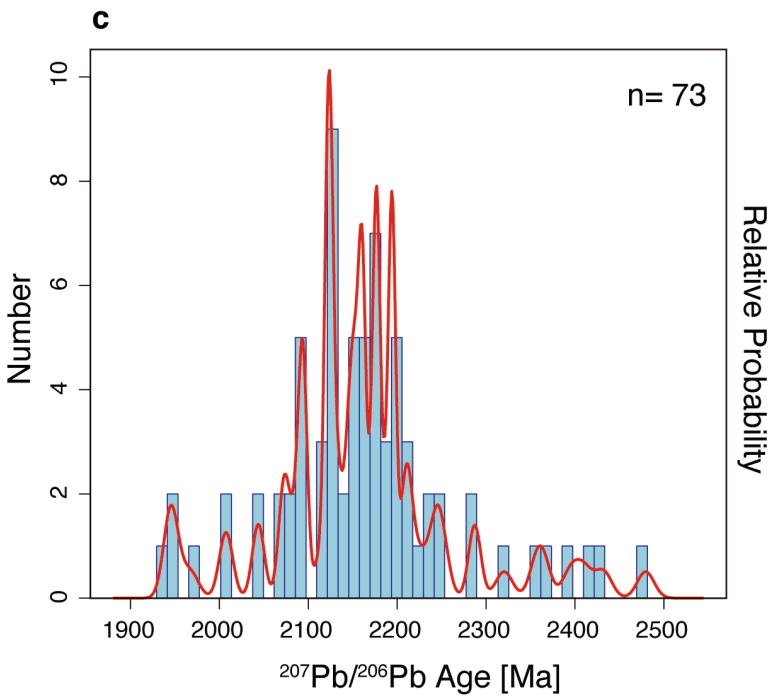
c
n= 73
Number
Relative Probability
0
2
4
6
8
10
1900
2000
2100
2200
2300
2400
2500
207Pb/206Pb Age [Ma]

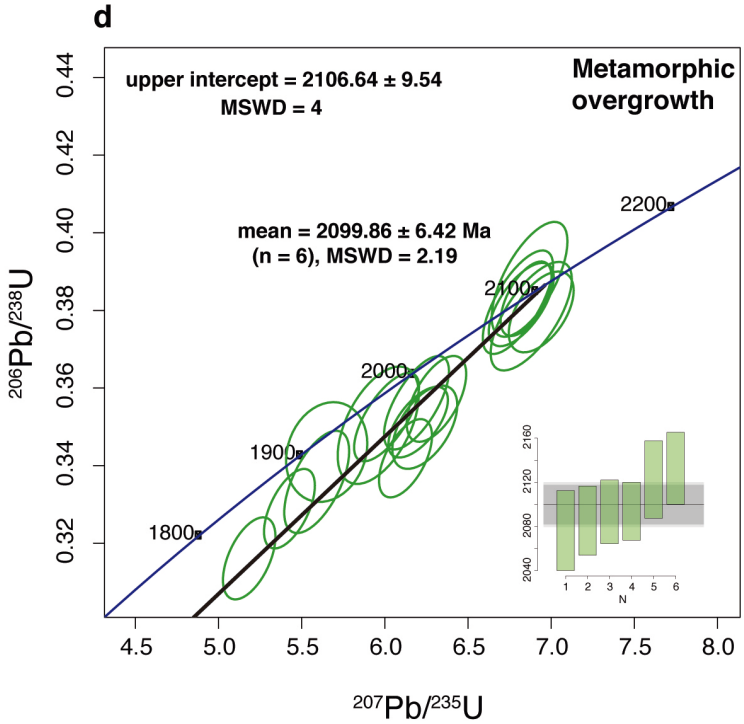
d
upper intercept = 2106.64 ± 9.54
MSWD = 4
Metamorphic
overgrowth
mean = 2099.86 ± 6.42 Ma
(n = 6), MSWD = 2.19
2200
2100
2000
1900
1800
0.32
0.34
0.36
0.38
0.40
0.42
0.44
4.5
5.0
5.5
6.0
6.5
7.0
7.5
8.0
206Pb/238U
207Pb/235U

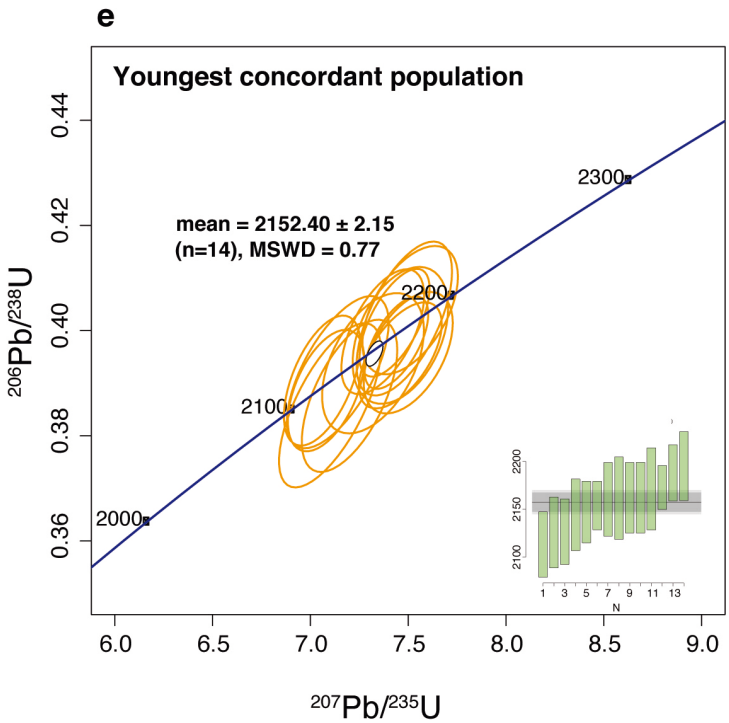
e
Youngest concordant population
mean = 2152.40 ± 2.15
(n=14), MSWD = 0.77
2300
2200
2100
2000
0.36
0.38
0.40
0.42
0.44
6.0
6.5
7.0
7.5
8.0
8.5
9.0
206Pb/238U
207Pb/235U

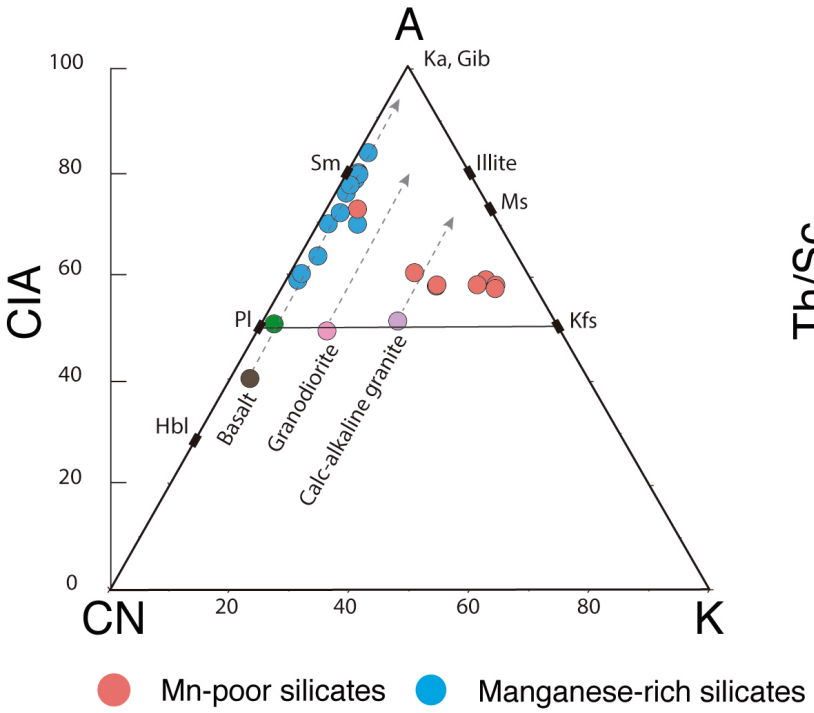

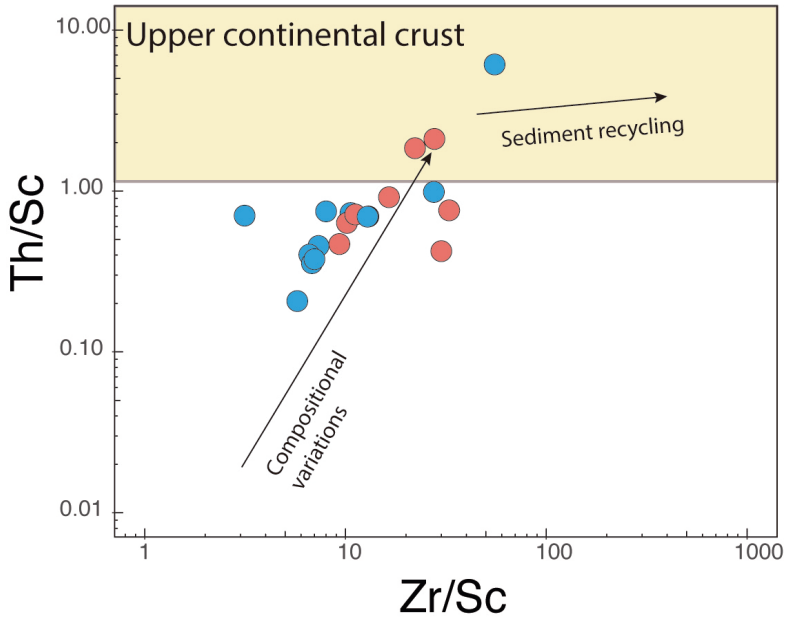

Mn-poor silicates Manganese-rich silicates

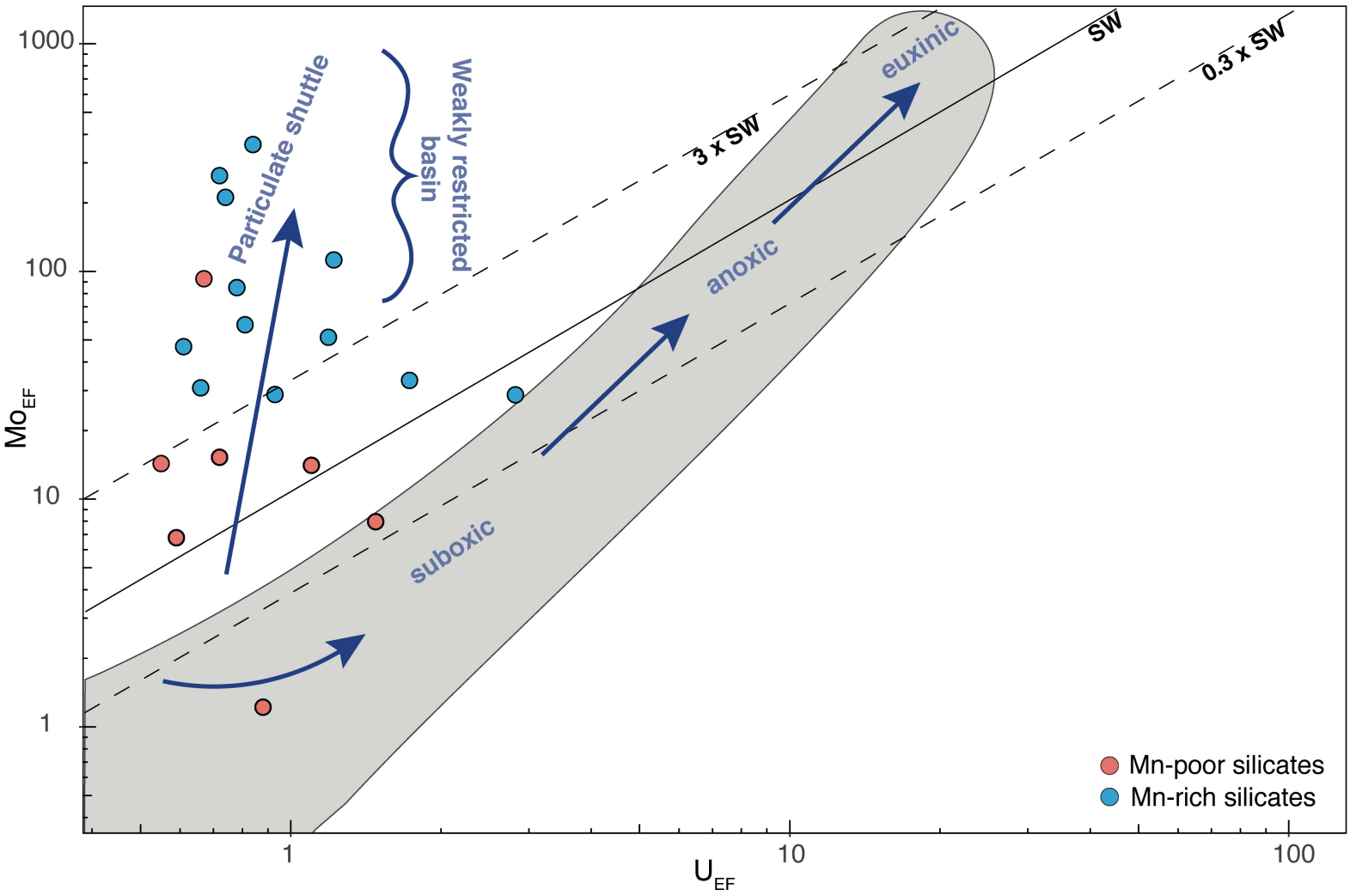
1000
100
10
1
Mo$_{EF}$
1
10
100
U$_{EF}$
Particulate shuttle
Weakly restricted basin
3 x SW
SW
0.3 x SW
euxinic
anoxic
suboxic
Mn-poor silicates
Mn-rich silicates

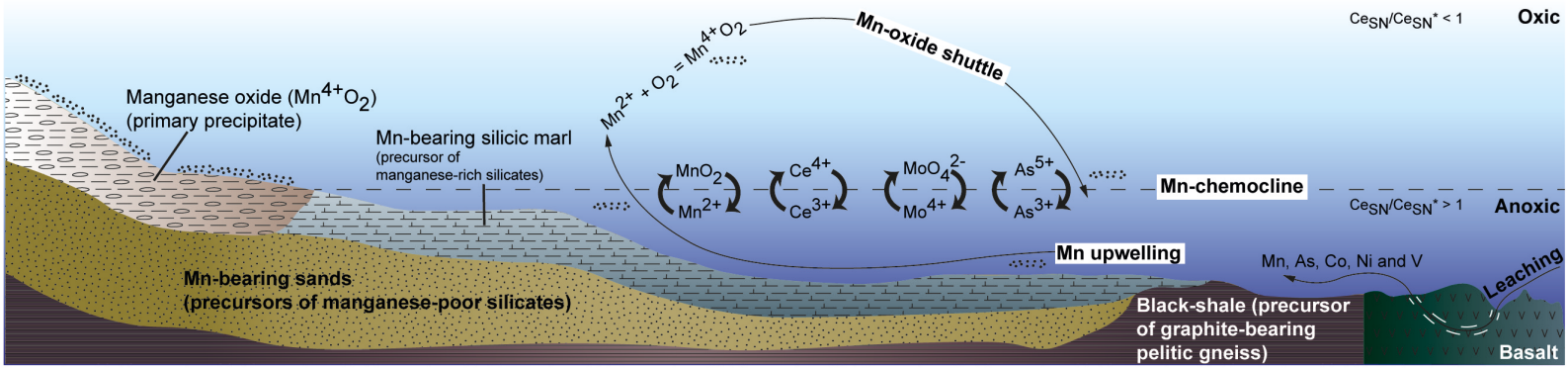
Oxic
$Ce_{SN}/Ce_{SN}^{*} < 1$
Manganese oxide ($Mn^{4+}O_2$)
(primary precipitate)
Mn-bearing silicic marl
(precursor of
manganese-rich silicates)
$Mn^{2+} + O_2 = Mn^{4+}O_2$
Mn-oxide shuttle
MnO_2
Mn^{2+}
Ce^{4+}
Ce^{3+}
MoO_4^{2-}
Mo^{4+}
As^{5+}
As^{3+}
Mn-chemocline
$Ce_{SN}/Ce_{SN}^{*} > 1$
Anoxic
Mn upwelling
Mn, As, Co, Ni and V
Leaching
Mn-bearing sands
(precursors of manganese-poor silicates)
Black-shale (precursor
of graphite-bearing
pelitic gneiss)
Basalt